

Materials Design Directions for Solar Thermochemical Water Splitting

Robert B. Wexler¹, Ellen B. Stechel² and Emily A. Carter^{1*}

¹*Department of Mechanical and Aerospace Engineering and the Andlinger Center for Energy and the Environment, Princeton University, Princeton, NJ, United States*

²*ASU LightWorks[®] and the School of Molecular Sciences, Arizona State University, Tempe, Arizona, United States*

Abstract

Solar thermochemical water splitting (STWS) offers a renewable route to hydrogen with the potential to help decarbonize several industries, including transportation, manufacturing, mining, metals processing, and electricity generation, as well as to provide sustainable hydrogen as a chemical feedstock. STWS uses high temperatures from concentrated sunlight or other sustainable means for high-temperature heat to produce hydrogen and oxygen from steam. For example, in its simplest form of a two-step thermochemical cycle, a redox-active metal oxide is heated to ≈ 1700 to 2000 K, driving off molecular oxygen while producing oxygen vacancies in the material. The reduced metal oxide then cools (ideally with the extracted heat recuperated for reuse) and, in a separate step, comes into contact with steam, which reacts with oxygen vacancies to produce molecular hydrogen while recovering the original state of the metal oxide. Despite its promising use of the entire solar spectrum to split water thermochemically, the estimated cost of hydrogen produced via STWS is ≈ 4 to $6\times$ the U.S. Department of Energy (DOE) Hydrogen Shot target value of $\$1/\text{kg}$.

One contributing approach to bridging this cost gap is the design of new materials with improved thermodynamic properties to enable higher efficiencies. The state-of-the-art (SOA) redox-active metal oxide for STWS is ceria (CeO_2) because of its close to optimal, although too high, oxygen vacancy formation enthalpy and large configurational and electronic entropy of reduction. However, ceria requires high operating temperatures, and its efficiency is insufficient. Therefore, efforts to increase the efficiency of STWS cycles have focused

*Corresponding author: eac@princeton.edu

on further optimizing oxygen vacancy formation enthalpies and augmenting the reduction entropy via substitution or doping and materials discovery schemes. Examples of the latter include the perovskites $\text{BaCe}_{0.25}\text{Mn}_{0.75}\text{O}_3$ and $(\text{Ca,Ce})(\text{Ti,Mn})\text{O}_3$. These efforts and others have revealed intuitive chemical principles for the efficient and systematic design of more effective materials, such as the strong correlation between the enthalpies of crystal bond dissociation and solid-state cation reduction with the enthalpy of oxygen vacancy formation, as well as configurational entropy augmentation via the coexistence of two or more redox-active cation sublattices.

The purpose of this chapter is to prepare the reader with an up-to-date account of STWS redox-active materials, both the SOA and promising newcomers, as well as to provide chemically intuitive strategies for improving their cycle efficiencies through materials design—in conjunction with ongoing efforts in reactor engineering and gas separations—to reach the cost points for commercial viability.

Keywords: Climate change, concentrated solar technologies, hydrogen, solar thermolysis, solar thermochemical cycles, redox-active materials, off-stoichiometric, quantum mechanics simulations

1.1 Introduction

Combatting anthropogenic climate change is one of the critical scientific and engineering challenges of our time. The associated global warming (Figure 1.1a)—predominantly brought about by greenhouse-gas emissions from burning fossil fuels [1–3]—already has led to extreme weather events that threaten the safety and food/water security of life on Earth. Averting the most disastrous effects of climate change calls—at least in part—for clean fuel alternatives to avoid the CO_2 emissions from hard-to-electrify sectors, including heavy-duty vehicles with petroleum-based combustion engines. One encouraging alternative is H_2 , which has a higher-energy density per unit mass than liquid hydrocarbons and can be produced using sustainable energy in the form of concentrated solar heat via thermolysis or thermochemical water splitting (Figure 1.1b) [4]. Although not reviewed here, H_2 can also be sustainably produced from water by alternative means, for example, via photoelectrochemical water splitting [5, 6] and both high- [7] and low-temperature [8] electrolysis employing renewable (or nuclear) energy. Concentrated solar technologies (CSTs) also promise to reduce the

carbon dioxide footprint of fossil-fuel-derived H_2 from steam-methane reforming, hydrocarbon (fossil or biomass) gasification, solid-oxide electrolysis, and methane cracking.

Two popular solar thermal collector/receiver/reactor designs are the tower with a heliostat field and the parabolic dish (Figure 1.1c) [9]. In the increasingly adopted solar power tower plant architecture, many heliostats focus sunlight on an elevated receiver, achieving a solar concentration ratio (C)—i.e., the factor by which a collector/receiver multiplies the intensity of sunlight impinging upon the Earth's surface—of ≈ 1000 . For parabolic dishes, a polished metal mirror lining concentrates sunlight on a focal point, where redox-active materials could be heated to high temperatures (e.g., 1700–1800 K [10]). While dishes currently are more expensive than towers, they generally lead to a higher C [11] and recently have been used in demonstration CST-based systems [10].

The theoretical maximum efficiency of solar-to- H_2 conversion using CSTs is—under the assumption of ideal optics and a perfectly insulated receiver—the product of the solar collector, receiver, and reactor (Carnot) efficiencies [12, 13]

$$\eta_{solar-to-fuel} = \eta_{collector} \eta_{receiver} \eta_{Carnot} \quad (1.1)$$

$$\eta_{receiver} = 1 - \frac{\sigma T^4}{IC} \quad (1.2)$$

$$\eta_{Carnot} = 1 - \frac{T_{sur}}{T} \quad (1.3)$$

where σ is the Stefan–Boltzmann constant; T the temperature of the receiver; I the intensity of the direct, normal-incident sunlight; and T_{sur} is the temperature of the surroundings (e.g., 298.15 K). Suppose a heliostat field with a solar tower is used instead of a parabolic dish. In that case, $\eta_{collector}$ will be less than one due to factors including the cosine effect (i.e., due to heliostats not pointing directly at the sun and the receiver simultaneously, hence, there is a reduction in the effective reflection area) [14]. One can think of the receiver efficiency ($\eta_{receiver}$) as the fraction of absorbed

6 SOLAR FUELS

sunlight that is not reradiated by the blackbody-like receiver. Increasing C can increase the T range over which η_{receiver} is close to 100%. For example, if parabolic dishes—with C reaching 10000—can be made economical, then a nearly perfect receiver can be achieved at ≈ 2000 K (Figure 1.1d,

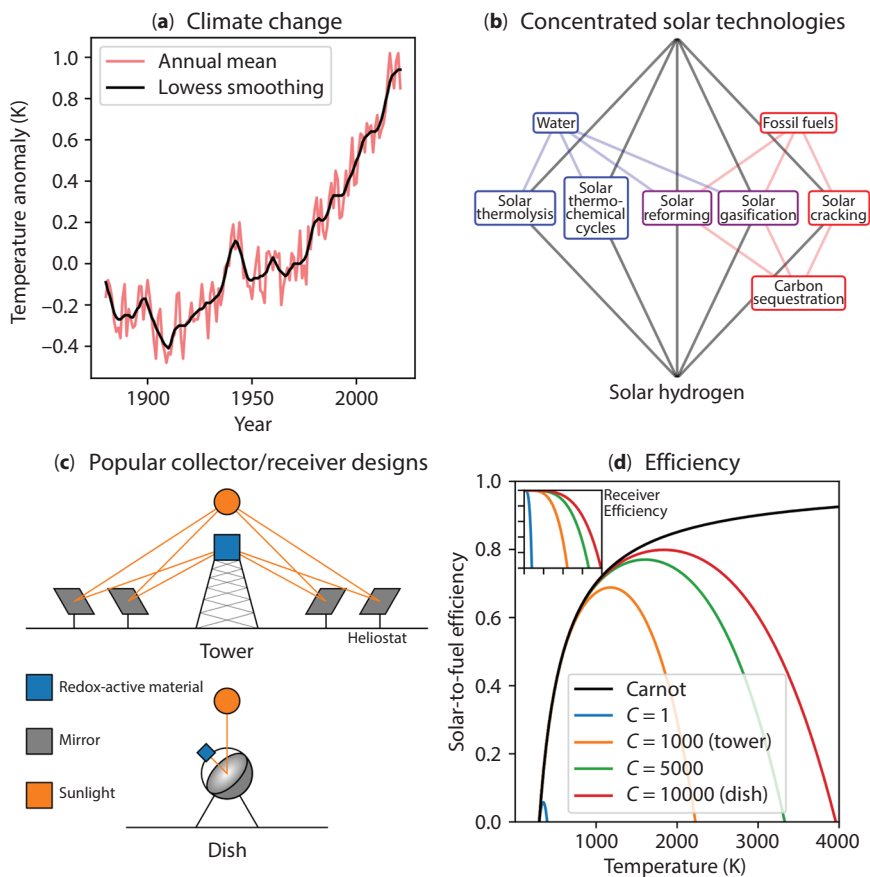
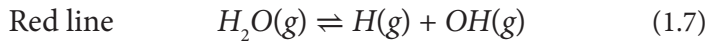
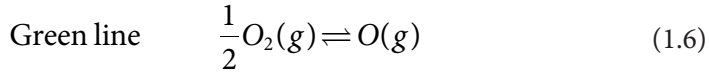
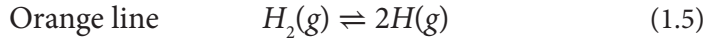
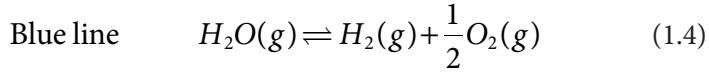


Figure 1.1 Concentrated solar hydrogen for combatting climate change. (a) Increase in global temperature since 1880. (b) Routes to solar hydrogen via concentrated solar technologies. (c) Popular collector/receiver designs for concentrated solar heat technologies. (d) Ideal solar-to-fuel efficiency ($\eta_{\text{solar-to-fuel}}$ in Equation (1.1)) and (d, inset) receiver efficiency (η_{receiver} in Equation (1.2))—with the same ticks and tick labels as the larger panel). Note that towers can have $C > 1000$ and developing dishes with $C = 10,000$ is quite challenging. That said, we chose these values to indicate the effect of order-of-magnitude changes in C on the theoretical solar-to-fuel efficiency.

inset). While η_{receiver} dominates $\eta_{\text{solar-to-fuel}}$ in the high-temperature limit, the efficiency of a Carnot engine (η_{Carnot}) governs the low-temperature regime, which decreases to zero as T approaches T_{sur} from above. Upon multiplying these three efficiencies, it becomes clear that—for a given C —there is an ideal temperature at which $\eta_{\text{solar-to-fuel}}$ is maximized (Figure 1.1d). As an example, consider a dish that provides $C = 5000$. If the receiver is heated to 1800 K, one can use $\leq 76\%$ of the concentrated sunlight energy for solar-to- H_2 conversion. Here, the “less than” indicates that other loss mechanisms and engineering constraints typically produce efficiencies $\ll 76\%$.

1.1.1 Hydrogen via Solar Thermolysis

Having introduced CSTs and their efficiencies for a general solar-to- H_2 process, we now consider the earliest and perhaps simplest approach to CST-based hydrogen production via solar thermolysis or *direct* solar water splitting [15]. In solar thermolysis, $\text{H}_2\text{O}(\text{g})$ is heated to $T \geq 2500$ K, above which it can undergo the following high-temperature reactions (Figure 1.2a) [16]:



At $T < 2000$ K and $p = 1$ bar, none of these reactions occur with appreciable yields, leaving $\text{H}_2\text{O}(\text{g})$ intact (Figure 1.2b). As T reaches 2500 K, $\approx 4\%$ of $\text{H}_2\text{O}(\text{g})$ molecules split into $\text{H}_2(\text{g})$ and $\text{O}_2(\text{g})$ (Equation 1.4). For $T > 2500$ K, however, side reactions—such as the atomization of $\text{H}_2(\text{g})$ (Equation 1.5) and $\text{O}_2(\text{g})$ [Equation (1.6)], and the dissociation of $\text{H}_2\text{O}(\text{g})$ into $\text{H}(\text{g})$ and $\text{OH}(\text{g})$ (Equation 1.7)—compete with the desired water-splitting reaction, leading to a maximum $\text{H}_2(\text{g})$ mole fraction of ≈ 0.19 at 3400 K. In addition to its upper limit for H_2 generation, solar thermolysis is impractical [17] because it produces an explosive mixture of $\text{H}_2(\text{g})$ and $\text{O}_2(\text{g})$ that requires careful separation and rapid quenching to avoid recombination, which reduces efficiency. Furthermore, the T needed to produce $\text{H}_2(\text{g})$ and not

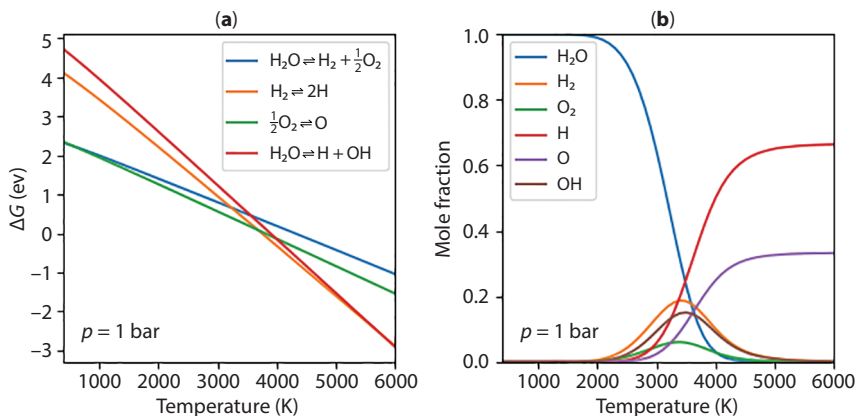
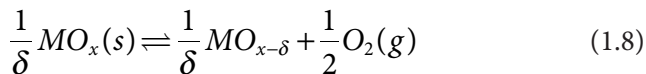


Figure 1.2 Thermodynamics of hydrogen production via solar thermolysis. (a) Gibbs free energy change (ΔG) of high-temperature reactions at $p = 1$ bar. (b) Equilibrium mole fractions at $p = 1$ bar (see Appendix A. Equilibrium Composition for Solar Thermolysis).

$\text{H}(\text{g})$ or $\text{OH}(\text{g})$ —i.e., ≈ 2500 K—leads to the thermal failure of the ceramics used for $\text{H}_2(\text{g})$ and $\text{O}_2(\text{g})$ separation, thus motivating—in the absence of solutions for these issues—another route to solar H_2 , namely solar thermochemical water splitting (STWS) [18–26].

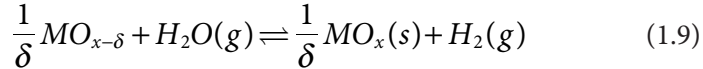
1.1.2 Hydrogen via Solar Thermochemical Cycles

To split water at lower temperatures and preclude the formation of undesired gas-phase molecules, one can employ thermochemical cycles, the simplest of which—and the primary subject of this book chapter—is a two-step cycle [27–34] (Figure 1.3a) with redox-active, metal-oxide materials (Figure 1.3b). In such a cycle, a metal oxide (MO_x , where x is the number of moles of O per cation) first is heated, using CSTs, to temperatures typically exceeding 1500 K and most often close to 1800 K, at which point it is reduced to a more O-poor stoichiometry ($\text{MO}_{x-\delta}$), i.e.,



where δ is the off-stoichiometry; note that we have purposefully omitted the phase of the reduced metal oxide for reasons to be explained momentarily. Generally speaking, one would reduce at the highest temperatures within engineering and economic constraints to ensure maximal reduction

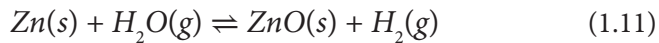
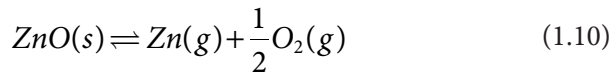
(as increasing the temperature makes ΔG more negative and therefore increases δ) and fast kinetics. In the second step, the reduced metal oxide cools to a temperature where reoxidation is possible when exposed to $H_2O(g)$, which leads to water splitting and regeneration of the original metal oxide, i.e.,



Generally, $MO_{x-\delta}$ will not reoxidize to the fully stoichiometric form MO_x but will cycle between two forms of the metal-oxide stoichiometry—both partially reduced—where the difference between the two off-stoichiometries is one of the performance metrics. The reoxidation is further limited if there is a small amount of hydrogen in the gas stream, which might be expected if one separates, in the gas phase, the hydrogen from the reoxidation product stream and recycles any unconverted steam.

Unlike thermal reduction (Equation 1.8), whose ideal operating temperature is bounded only from above by the thermal stability of the material and durability of the reactor, one would perform water splitting (Equation 1.9) at temperatures high enough for fast kinetics but low enough for a good ΔG of reoxidation. This compromise often requires water splitting to be done around 1000 K or higher. Another consideration is recuperation of heat between the high temperature and low temperature steps. The larger the temperature difference, the greater the engineering challenge to limit the losses.

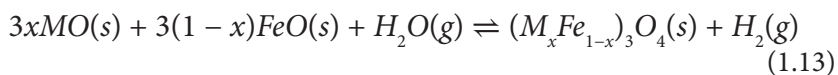
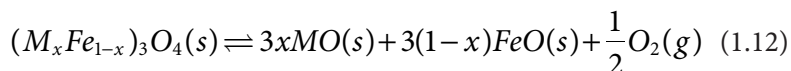
Until now, we have neither specified the phase of $MO_{x-\delta}$ nor the extent of reduction δ . Two-step metal-oxide thermochemical cycles are based on either volatile or non-volatile metal oxides. Volatile refers to a metal oxide for which a solid-to-gas phase transition accompanies thermal reduction. One of the most widely studied volatile cycles is $ZnO(s)/Zn(g)$ [35–37]:



In the thermal reduction step [Equation (1.10)], which one must carry out at temperatures above 2000 K, $ZnO(s)$ volatilizes to $Zn(g)$ and $O_2(g)$. While the $ZnO(s)/Zn(g)$ cycle offers favorable efficiencies even in the

absence of heat recovery (energy conversion efficiency $\approx 45\%$ and maximum exergy efficiency $\approx 29\%$), its issues are similar to those faced in solar thermolysis in that the high temperatures required for significant reduction put a considerable thermal strain on the receiver/reactor [17, 38]. After thermal reduction, one generally quenches quickly to avoid the back reaction before separating Zn(s) from O₂(g). Alternatively, electrothermal gas-phase separation has been considered [39, 40]. Water splitting [Equation (1.11)], on the other hand, typically takes place at $T \leq 900$ K, revealing another difficulty for ZnO(s)/Zn(g): the need for a giant temperature swing (≥ 1100 K). Other redox couples for volatile, two-step STWS have been considered, such as post-transition-metal oxides in the SnO₂(s)/SnO(g) cycle [41–43]; however, those with greater attention currently are solid phase, a.k.a. non-volatile, redox-active materials.

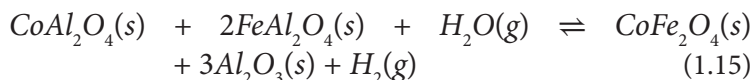
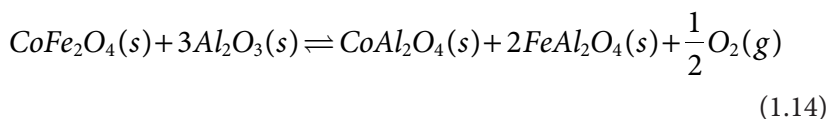
Within non-volatile, redox-active metal oxides, the two main categories are stoichiometric (line compounds) and off-stoichiometric. First, we consider stoichiometric metal oxides, where stoichiometric refers to materials for which reduction and reoxidation produce pure, solid-phase, metal-containing compounds obeying full stoichiometry constraints on composition. One can further subdivide stoichiometric metal oxides into single-component and multi-component compositions. Examples best illustrate the difference between these two types of stoichiometric oxides. The prototypical single-component materials are metal-doped ferrites [44–54], whose thermal reduction and water splitting reactions are



where the metal (M) dopant or substituent can be Fe (in which case Fe is not a dopant and the phase is magnetite) [55–59], Zn [60], Ni [60, 61], Co [60, 62] (as well as a complete replacement of Fe with Co [63]), Mn [61], and others. Ferrites with other metals substituted in the spinel or inverse spinel structure can be tuned to provide nearly optimal reduction Gibbs free energetics and reduction temperatures lower than 2000 K [64, 65]. However, both their reduction and water-splitting kinetics are slow because O²⁻ is close-packed in both oxide structures, Fe₃O₄ and FeO(s). Therefore, it does not react beyond the surface [66]. Additionally, powdered Fe oxides sinter, rendering them uncyclable [56, 62, 67, 68]. To enhance cyclability,

one can use yttria-stabilized zirconia as an inert support that incorporates active Fe ions into its crystal lattice, forming a solid solution, thus alleviating the sintering or melting of iron oxides at the working temperatures of 1200 to 1700 K [55, 69]. Note that, for ferrite cycles, a single metal oxide reduces and reoxidizes, hence the terminology “single component.”

Alternatively, multi-component cycles involve the redox of more than one metal oxide component. An excellent example of this case is the cycle based on the mineral hercynite $\text{FeAl}_2\text{O}_4(\text{s})$ [70–77]:



During thermal reduction, $\text{CoFe}_2\text{O}_4(\text{s})$ —a metal-substituted ferrite—reacts with three moles of $\text{Al}_2\text{O}_3(\text{s})$, producing $\text{CoAl}_2\text{O}_4(\text{s})$ —a pigment known as cobalt blue—along with two moles of hercynite and a half mole of $\text{O}_2(\text{g})$. These intermediate products then split water at lower temperatures, restoring the original solids in their starting stoichiometric coefficients and generating $\text{H}_2(\text{g})$. Both steps have two metal-oxide components in the reactants and products, so the hercynite cycle is multi-component. However, like the ferrites, this cycle suffers from poor kinetics, which is unsurprising considering one of the components is cobalt ferrite $\text{CoFe}_2\text{O}_4(\text{s})$. Other studied multicomponent cycles include—but are not limited to—those based on the metal sulfate/oxide [e.g., $\text{MnSO}_4(\text{s})/\text{MnO}(\text{s})$ [78]] and metal dioxide/pyrochlore [i.e., $\text{CeO}_2(\text{s})+\text{MO}_2(\text{s})/\text{Ce}_2\text{M}_2\text{O}_7(\text{s})$ where M can be, e.g., Ti [79], Si [79], or Sn [80]] redox couples. Ultimately, kinetic limitations are a hallmark of stoichiometric materials because their STWS cycles require the nucleation and growth of bulk phases. A promising path to promote faster kinetics is to use off-stoichiometric metal oxides, which tend to be mixed ionic-electronic conductors (MIECs) that form and fill oxygen vacancies ($\text{V}_{\text{O}}\text{s}$) during thermal reduction and water splitting, respectively, instead of undergoing major bulk structural phase transitions. As off-stoichiometric metal oxides, particularly MIECs because of their superior ion diffusion kinetics, currently are the subject of intense research for STWS applications and are the redox-active materials of choice for pilot plants, we focus on them here. Below we emphasize developing intuition that explains observed physicochemical phenomena, in order to determine

materials design criteria that can lead to tailoring materials for more optimal thermochemical cycles.

Before we dive into the details of off-stoichiometric metal oxides for STWS, we would be remiss if we did not mention the utility of multi-step cycles. We will first describe the Cu-Cl [81] cycle (Figure 1.3c). In the hydrolysis step, $\text{Cu(II)Cl}_2(\text{s})$ is heated to ≈ 673 K in the presence of $\text{H}_2\text{O}(\text{g})$,

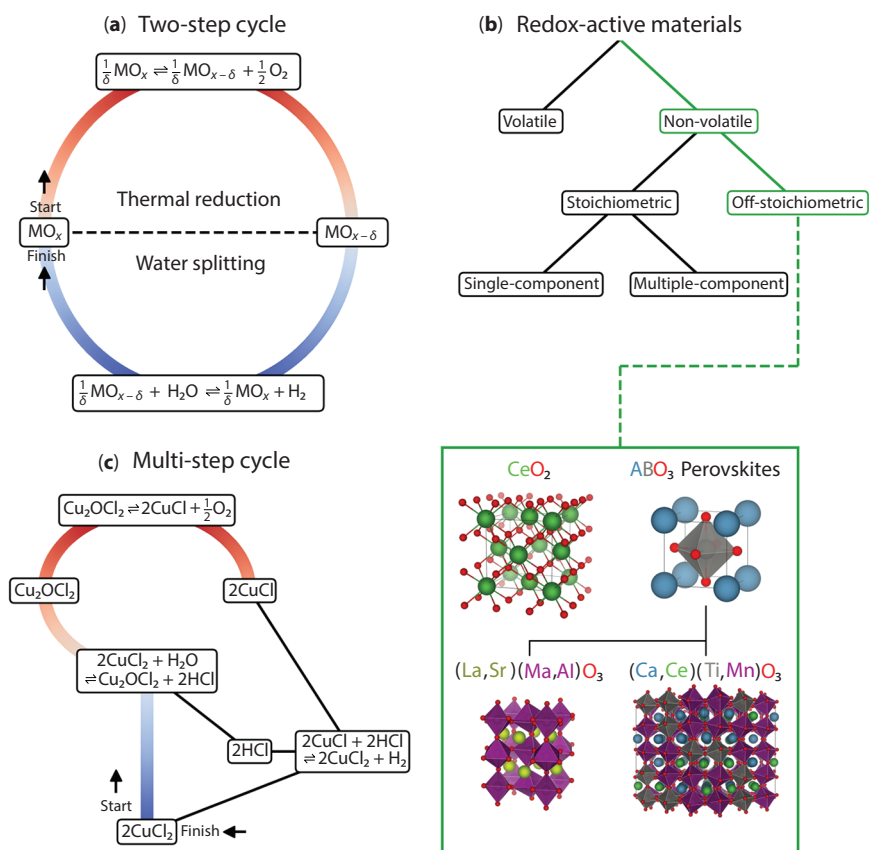


Figure 1.3 Hydrogen production via solar thermochemical cycles. (a) Schematic of a two-step cycle for a metal oxide (MO_x) that becomes off-stoichiometric ($\text{MO}_{x-\delta}$, where δ is the off-stoichiometry) upon thermal reduction (where the color of the circle denotes relative temperature). (b) Types of redox-active materials typically employed for two-step STWS, where our focus is on nonvolatile materials that become off-stoichiometric upon thermal reduction, such as CeO_2 and ABO_3 perovskites and their alloys. (c) Schematic of a multistep cycle, specifically, here, the copper chloride hybrid cycle, which involves hydrolysis (blue), thermal reduction (red), and electrolysis (black) steps at different temperatures.

forming melanothallite $\text{Cu(II)}_2\text{OCl}_2(\text{s})$ and $\text{HCl}(\text{g})$. Then, in the thermal reduction step, $\text{Cu(II)}_2\text{OCl}_2(\text{s})$ is solar heated to ≈ 773 K using CSTs, which leads to its reductive decomposition into $\text{Cu(I)Cl}(\text{s})$ and $\text{O}_2(\text{g})$. One can liken this step to the thermal reduction step in the two-step STWS cycles described above. Last is the electrolysis step, where $\text{HCl}(\text{g})$ from hydrolysis and $\text{Cu(I)Cl}(\text{s})$ from thermal reduction react at ambient temperatures and under the application of an oxidizing electrode potential, producing $\text{H}_2(\text{g})$ and regenerating Cu(II)Cl_2 for subsequent cycles. While the Cu-Cl cycle enables efficient heat recycling and offers lower operating temperatures than two-step cycles, solids handling between steps and corrosive chemical components—in addition to the difficulties associated with engineering a multi-step engine with compounding inefficiencies—challenge the practical application of the multi-step Cu-Cl cycle, as well as others, including the hybrid sulfur [$\text{H}_2\text{SO}_4(\text{aq})/\text{SO}_2(\text{g})$] [82–84] and sulfur-iodine cycles [85–87]. As a final remark, we acknowledge that the preceding discussion represents a limited survey of cycles and redox-active materials. There have been >300 cycles screened [19, 88]. However, since several seminal articles offer a more comprehensive overview [22, 25, 33], we truncate here our consideration of either stoichiometric or line compounds (volatile and non-volatile materials) or multi-step or hybrid cycles.

1.1.3 Thermodynamics

One of the most critical constraints for two-step solar-thermochemical cycles [14, 89–96] with off-stoichiometric metal oxides is the thermodynamic spontaneity of the thermal reduction and water splitting reactions [97, 98]. For reversible/equilibrium thermal reduction [Equation (1.8)], the Gibbs free energy change for an infinitesimal change in the off-stoichiometry $d\delta$ in a counter-current reactor [99–101] is

$$\begin{aligned}\Delta G_{red} &= \frac{1}{d\delta} \left(G_{\text{MO}_{x-\delta-d\delta}}^{\circ} - G_{\text{MO}_{x-\delta}}^{\circ} \right) + \frac{1}{2} G_{\text{O}_2}^{\circ} + \frac{1}{2} RT_{red} \ln \left(\frac{p_{\text{O}_2}^{red}}{p^{\circ}} \right) \\ &= \Delta G_v^{\circ} + \frac{1}{2} RT_{red} \ln \left(\frac{p_{\text{O}_2}^{red}}{p^{\circ}} \right) = 0\end{aligned}\quad (1.16)$$

where G (G°) is the (standard) Gibbs free energy, R is the universal gas constant, T_{red} is the thermal reduction temperature, $p_{\text{O}_2}^{red}$ is the inlet partial

pressure of $O_2(g)$ for the thermal reduction reaction at T_{red} , p° is the reference pressure (1 bar), and

$$\Delta G_v^\circ = \frac{1}{d\delta} (G_{MO_{x-\delta-d\delta}}^\circ - G_{MO_{x-\delta}}^\circ) + \frac{1}{2} G_{O_2}^\circ = \Delta H_v^\circ - T_{red} \Delta S_v^\circ \quad (1.17)$$

ΔG_v° , ΔH_v° , and ΔS_v° are the standard V_O formation Gibbs free energy, enthalpy, and entropy at an oxygen partial pressure of p , respectively, which depend on δ (for simplicity, we omit this dependence). Figure 1.4a shows combinations of ΔH_v° and T_{red} that satisfy $\Delta G_{red} = 0$ for $p_{O_2}^{red} = 1 \times 10^{-4}$ bar. One can read this graph as follows. For example, if a redox-active material has a T -independent $\Delta S_v^\circ = 15 k_B$ and $\Delta H_v = 3$ eV, $T_{red} \approx 1800$ K or above is required for thermal reduction. In other words, the intersection of an isoenthalpic (constant- ΔH_v°) line with a vertical line passing through ΔS_v° gives the minimum reduction temperature.

For water splitting (Equation 1.9), the Gibbs free energy change is

$$\Delta G_{ox} = \frac{1}{d\delta} (G_{MO_{x-\delta}}^\circ - G_{MO_{x-\delta-d\delta}}^\circ) + G_{H_2}^\circ - G_{H_2O}^\circ + RT_{ox} \ln \left(\frac{p_{H_2}^{ox}}{p_{H_2O}^{ox}} \right) \quad (1.18)$$

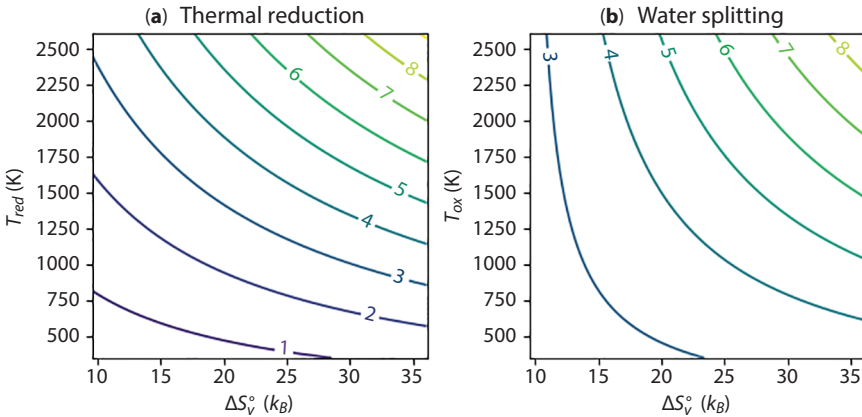


Figure 1.4 Thermodynamics of hydrogen production via a two-step solar-thermochemical cycle at (a) $p_{O_2}^{red} = 1 \times 10^{-4}$ bar for thermal reduction and (b) $\theta = 0.1$ for water splitting. The different curves are isoenthalpic lines, and the numbers (colors) are (correspond to) ΔH_v° in eV. Spontaneous reaction may occur for T_{red} above the isoenthalpic lines for a given ΔH_v° .

where T_{ox} is the reoxidation temperature, and $p_{H_2}^{ox}$ and $p_{H_2O}^{ox}$ are the outlet partial pressures of $H_2(g)$ and $H_2O(g)$, respectively, for the water-splitting reaction at T_{ox} . To obtain ΔG_{ox}^o in terms of ΔG_v^o , we consider the Gibbs free energy change of gas-phase water splitting [Equation (1.4)], i.e.,

$$\Delta G_{ws}^o = G_{H_2}^o + \frac{1}{2}G_{O_2}^o - G_{H_2O}^o = -RT_{ox} \ln K_{ws} \quad (1.19)$$

Here, K_{ws} is the equilibrium constant of water splitting (abbreviated ws). Substituting this result into Equation (1.18) and using the definition of ΔG_v^o [Equation (1.17)], one arrives at the following equality for reversible/equilibrium ΔG_{ox}^o :

$$\Delta G_{ox}^o = -\Delta G_v^o - RT_{ox} \ln \left(\frac{1-\theta}{\theta} K_{ws} \right) = 0 \quad (1.20)$$

Note that we have replaced $p_{H_2}^{ox}/p_{H_2O}^{ox}$ with $\theta/(1-\theta)$, where θ is the outlet H_2/H_2O conversion ratio. For example, if we begin with one mole of $H_2O(g)$ and the reaction proceeds 10 %—i.e., with $\theta = 0.1$ —then we end with $1-\theta = 0.9$ or 0.9 moles of $H_2O(g)$ and 0.1 moles of $H_2(g)$. For off-stoichiometric metal oxides, $\theta = 0.1$ is a reasonable target value for the water-splitting step [98]. To explore the thermodynamics of water splitting graphically, Figure 1.4b shows the relationship between T_{ox} (vertical axis), ΔS_v^o (horizontal axis), and ΔH_v^o (colors and numbers). The curvature of the $\Delta H_v^o = 3 \text{ eV}$ isoenthalpic line indicates that T_{ox} depends very sensitively on ΔS_v^o , with values ranging from $\approx 600 \text{ K}$ to $\approx 1800 \text{ K}$ for $\Delta S_v^o = 17 k_B$ and $12 k_B$, respectively. Therefore, modulating T_{red} and T_{ox} demands careful control of the material-specific parameters, ΔH_v^o and ΔS_v^o . Based on the water-splitting isoenthalpic lines in Figure 1.4b, it is clear that—to ensure practical temperatures and temperature swings— ΔH_v^o must be between 3 eV and 4 eV for metal oxides with typical ΔS_v^o s of 12–17 k_B . Solving Equations (1.16), (1.17), and (1.20) for ΔH_v^o gives

$$\Delta H_v^o = \frac{RT_{red} \ln \left[(1-\theta)\theta^{-1} K_{ws} \left(p^o / p_{O_2}^{red} \right)^{1/2} \right]}{1 - T_{red}/T_{ox}} \quad (1.21)$$

If one selects the target reducing conditions $T_{red} = 1800 \text{ K}$ and $p_{O_2}^{red} = 1 \times 10^{-4}$ to 1×10^{-3} bar and reoxidizing conditions $T_{ox} = 1200 \text{ K}$ and

$\theta = 0.1$, then the optimal ΔH_v° is 3.5 to 3.9 eV at $p^\circ = 1$ bar and $K_{ws}(T_{ox} = 1200 \text{ K}) = 1.2582 \times 10^{-8}$ [16].

The amount of $\text{H}_2(\text{g})$ produced from one mole of $\text{MO}_{x,\delta}$ and one mole of water in a cycle depends on both δ and θ [102–104], where δ is the number of moles of O that one mole of the metal oxide can extract from $\text{H}_2\text{O}(\text{g})$ after thermal reduction and θ is the conversion yield of water. One can measure δ by thermogravimetric analysis or coulometric titration [105–109]. For the former, one measures the mass of a sample over time as the temperature and partial pressure of oxygen changes. For the latter, one uses a constant current system to quantify the partial pressure of $\text{O}_2(\text{g})$ accurately.

Kinetics also place important constraints on the design of STWS applications [110–116]. For example, low temperatures (assuming the reoxidation reaction is exothermic) improve the thermodynamics of water splitting [33] but lead to sluggish kinetics and therefore suppress the rate of $\text{H}_2(\text{g})$ production. High temperatures alleviate these kinetics issues but disfavor the spontaneity and conversion yield of water splitting. According to Equation (1.16), reducing $p_{\text{O}_2}^{\text{red}}$ reduces T_{red} for the same reduction extent. There are two ways to reduce $p_{\text{O}_2}^{\text{red}}$, inert gas (N_2 or Ar) sweeping [101] and vacuum pumping [117], and each has its own challenges.

1.1.4 Economics

Before describing metal-oxide design directions, it is essential to consider the economics of STWS [118, 119]. The U.S. DOE recently designated the Hydrogen Shot target to be \$1/kg for clean H_2 within a decade, which—if achieved—could lead to a five-fold increase in hydrogen use and mostly from clean hydrogen. One estimate in a technoeconomic assessment [119] of a plant co-producing hydrogen and electricity with ceria as the redox-active material suggests an n^{th} of a kind commercial scale plant might produce H_2 at a cost of \$4.55/kg. In that study, component prices (e.g., $\approx \$22,500,000$ for a single 27.74 MW tower system) contributes $\approx 9.63\%$ of the cost. The \$4.55/kg H_2 is more than four times the target value. For hybrid cycles, where excess heat produces electricity, opportunities exist to decrease cost by increasing solar field efficiency, increasing revenue from electricity, and reducing the financial capital recovery factor. Capitalizing on these opportunities and others mentioned in a recent technoeconomic analysis by one of the authors [119], a realistic estimate of the minimum cost achievable, in the absence of some unforeseen technological disruption, is \$2.09/kg H_2 .

One way to decrease the price of $\text{H}_2(\text{g})$ from STWS is to avoid the costs associated with the temperature swing between thermal reduction and water splitting (i.e., $\Delta T = T_{\text{red}} - T_{\text{ox}} \neq 0$) via isothermal [120–122] cycles, i.e.,

where $\Delta T = 0$. However, a recent analysis by Bayon *et al.* indicates that such cycles require operation at $T_{red} = T_{ox} \approx 2030$ K and utilization of redox-active metal oxides with specific values of ΔH_v^0 and ΔS_v^0 [98]. Another strategy to reduce the cost of solar thermochemical $H_2(g)$ is to design, e.g., using quantum mechanics simulation techniques, new redox-active materials that are composed of more abundant elements and provide ideal thermochemical characteristics that, for off-stoichiometric metal oxides, include an optimal oxygen vacancy formation energy $E_v \approx \Delta H_v^0$ [for a greater reduction extent, δ , than ceria and therefore $H_2(g)$ productivity [95] per unit of redox-active material] and a tunable ΔS_v^0 , which—like E_v —improves δ and $H_2(g)$ productivity but also controls ΔT and thus works to meet the challenge of solid-solid heat recuperation.

1.2 Theoretical Methods

Going forward, the main emphases of this chapter are two-fold: (1) to introduce state-of-the-art and next-generation off-stoichiometric redox-active metal oxides and to explain what has made them effective or promising and (2) to outline how one might go about designing superior off-stoichiometric metal-oxide materials for two-step STWS. For the latter, many of the strategies we will outline for the redox-active material's design draw on insights from quantum mechanics simulations. Generally speaking, this endeavor requires quantum mechanics because the off-stoichiometric metal oxides for two-step STWS typically contain both ionic and covalent bonds (where

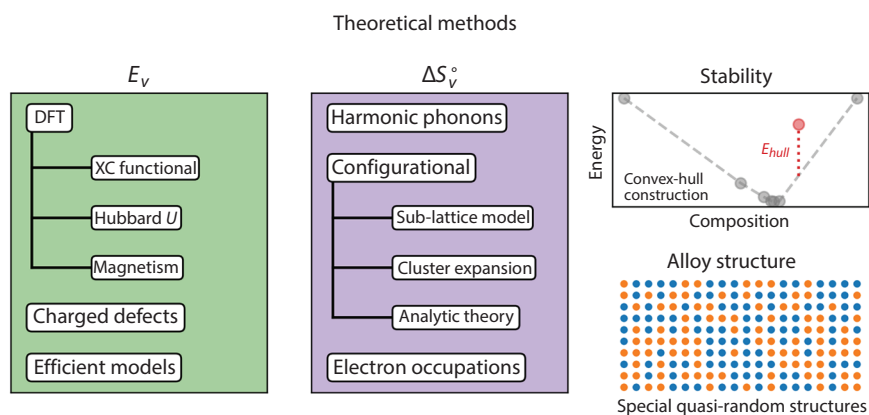


Figure 1.5 Theoretical methods for modeling redox-active metal oxides for STWS. Considerations when computing ΔG_v^0 , broken down by E_v , ΔS_v^0 , materials bulk stability, and structure. Each subtopic is addressed in the text.

the latter, of course, have a quantum mechanical origin), and redox-active transition metal cations (which exhibit quantum mechanical effects, such as crystal-field energy-level splitting and magnetism). Computational designers of metal oxides that undergo partial thermal reduction have four goals (Figure 1.5): (1) optimize E_v [97], (2) tune ΔS_v° , (3) control stability (which also applies for metal oxides that undergo stoichiometric thermal reduction), and (4) construct a realistic structural model (which is especially important for alloys).

1.2.1 Oxygen Vacancy Formation Energy

The first goal necessitates an accurate method for calculating E_v . The method of choice is density functional theory (DFT), for which its foundational theorems prove that one can express the total energy of a quantum mechanical system in its ground state simply as a functional of the electron density (n), a function of only three spatial coordinates. However, to obtain accurate electron kinetic energies, its usual implementation introduces one orbital for each electron, raising the complexity to be a function of $3N$ coordinates where N is the number of electrons and with an algorithmic scaling of typically $\sim N^3$. By contrast, conventional algorithms for more exact many-body-wavefunction methods for directly solving the Schrödinger equation scale typically as N^5 - N^7 . DFT approximations provide an accuracy-efficiency compromise for routinely computing total energy and enthalpy changes for chemical reactions and materials of up to a few hundred atoms at 0 K and for all species in their electronic ground states. There are four terms in the DFT energy functional,

$$E[n] = \int d\mathbf{r} n(\mathbf{r})V_n(\mathbf{r}) - \sum_i \int d\mathbf{r} \phi_i^*(\mathbf{r}) \frac{\nabla^2}{2} \phi_i(\mathbf{r}) + \frac{1}{2} \iint d\mathbf{r} d\mathbf{r}' \frac{n(\mathbf{r})n(\mathbf{r}')}{|\mathbf{r} - \mathbf{r}'|} + E_{xc}[n] \quad (1.22)$$

where $n(\mathbf{r})$ is the electron density, V_n is the nuclear potential, i is the electron index, ϕ are the one-electron wavefunctions (required because the exact kinetic energy density functional is unknown), and ∇ is the Laplacian. The first three terms deal with the classical electrostatic attraction between electrons and nuclei, the quantum mechanical kinetic energy of the electrons, and the classical electrostatic repulsion between electrons,

respectively. However, the exact form of the final term, which describes electron exchange and correlation (or XC), is unknown, so approximations are necessary and always must be validated for the systems of interest.

A logical starting point for developing XC functionals [123–125] is to assume that $E_{xc} = E_x + E_c$ is that of the homogeneous electron gas, i.e., homogeneously distributed electrons in a box. This local density approximation (LDA) is helpful because an exact analytic expression and numerical solution exist for E_x and E_c , respectively. However, the actual electron density has curvature, especially for materials with localized chemical bonds, high angular-momentum electrons, or defects. As a result, one should include information about the higher-order gradients of the electron density in constructing the XC functional. Perhaps the most widely used XC functional is based on the generalized gradient approximation (GGA) of Perdew, Burke, and Ernzerhof (commonly abbreviated as PBE [126]), which includes information about the electron density and its first derivative. Compared to the LDA, the PBE GGA dramatically improves predictions of the energetics of bond breaking and formation, which involves mostly localized electrons and therefore large gradients of the electron density at the reaction site. More recently, Sun *et al.* showed that inclusion of information about the second derivative of the electron density in the so-called strongly constrained and appropriately normed (SCAN) meta-GGA satisfies all 17 known XC constraints and provides remarkable accuracy for many solids [127].

DFT within the PBE GGA or SCAN meta-GGA, however, suffers from self-interaction errors (SIEs) not completely eliminated by the approximate XC functional that are introduced by the interaction of each electron with the entire electron density (including its own density) in the Coulomb energy functional. SIEs can lead to spurious delocalization of electrons, which is especially problematic for open-shell and redox-active transition metal compounds, whose d electrons can be localized and spin-polarized. To at least partly ameliorate the SIE, one can apply a Hubbard U correction to the DFT total energy, e.g., using the rotationally invariant approach introduced by Dudarev *et al.* [128], i.e.,

$$E_U[\{n_{mm}^{l\sigma}\}] = \sum_{l,\sigma} \frac{U^l}{2} \text{Tr}[\mathbf{n}^{l\sigma} (1 - \mathbf{n}^{l\sigma})] \quad (1.23)$$

where l and σ are the angular momentum and spin quantum numbers, $n_{mm}^{l\sigma}$ is a diagonal element of the on-site occupancy matrix \mathbf{n} , U_l is the effective

on-site Coulomb parameter, and Tr is the matrix trace of the quantity in brackets. Equation (1.23) can be understood as a total energy correction that drives the on-site occupancy matrix in the direction of idempotency, i.e., it penalizes noninteger electron occupation numbers. To correct the considerable error in the calculated redox reaction energies of many transition-metal oxides, which arises from the SIE in the PBE GGA, Wang *et al.* calibrated PBE+ U values for oxides containing the following transition metals: Co, Cr, Fe, Mn, Mo, Ni, V, and W [129]. Recently, one of the authors and her coworkers showed that the SCAN+ U [130, 131] framework more accurately reproduces the ground-state structure, lattice parameters, magnetic moments, and electronic properties of transition-metal oxides. We summarize the optimized U values for PBE+ U and SCAN+ U in Table 1.1. Since SCAN theoretically is a more accurate XC functional than PBE, i.e., it includes a more accurate description of electron exchange, it is not surprising that SCAN

Table 1.1 Hubbard U values for XC+ U calculations fit to relevant oxidation energies (unless otherwise noted). For example, the U value for SCAN+ U calculations of Ce oxides was fit to reproduce the experimental enthalpy of the following reaction: $4\text{CeO}_2(\text{s}) \rightleftharpoons 2\text{Ce}_2\text{O}_3(\text{s}) + \text{O}_2(\text{g})$. References are enclosed in brackets.

Element	PBE+ U (eV)	SCAN+ U (eV)
Sc	3.00 [138]	0 [131]
Ti	3.00 [138]	2.5 [131]
V	3.25 [129]	1 [131]
Cr	3.7 [129]	0 [131]
Mn	3.9 [129]	2.7 [130]
Fe	5.3 [129]	3.1 [130]
Co	3.32 [129]	3 [131]
Ni	6.2 [129]	2.5 [131]
Cu	3.6 (UHF-derived) [139]	0 [131]
Mo	4.38 [129]	n/a
W	6.2 [129]	n/a
Ce	2-3 [140, 141]	2 [130]

requires a lower U correction [132]. Transition-metal oxides also frequently exhibit magnetic degrees-of-freedom such as long-range magnetic order (ferromagnetic, antiferromagnetic, ferrimagnetic, and nonmagnetic) and local spin state (low, intermediate, and high), where the latter is especially relevant for compounds containing transition-metal cations, which can have varying d-electron counts and crystal-field splittings.

Armed with Hubbard- U -corrected DFT, one can compute E_v , which can be written as

$$E_v = E_{defect}^{supercell} - E_{bulk}^{supercell} + \frac{1}{2}E_{O_2} + q(E_F - \epsilon_{VBM}) + E_{corr} \quad (1.24)$$

where $E_{defect}^{supercell}$ and $E_{bulk}^{supercell}$ are the total energy—calculated using one’s preferred flavor of DFT XC and corrections—of a supercell with (defect) and without (bulk) the oxygen vacancy, E_{O_2} is the total energy of an $O_2(g)$ molecule, q is the charge of the defect (e.g., $q = 2$ for the removal of O^{2-}), $E_F - \epsilon_{VBM}$ is the Fermi energy relative to that of the valence band maximum (VBM), and E_{corr} fixes finite-size effects deriving from the use of periodic DFT and the supercell approach [133, 134]. The latter two terms only appear in the case of charged defects. A variety of correction procedures exist for the calculation of charged defects under periodic boundary conditions. In the state-of-the-art correction schemes proposed by Freysoldt, Neugebauer, and Van de Walle (FNV) [135], and Kumagai and Oba (KO) [136], they express E_{corr} as

$$E_{corr} = -E_{lat} + q\Delta\phi \quad (1.25)$$

where E_{lat} includes the interaction between the defect-induced charge density, the host material, and the neutralizing jellium (uniform compensating charge) background, and $\Delta\phi$ is a term that aligns the electrostatic potential of the defective and pristine materials with one produced by a model defect-induced charge density in an area of the material distant from the defect. The FNV procedure employs the plane-averaged electrostatic potential to calculate $\Delta\phi$, whereas the KO method uses atomic-site potentials. See ref [137] for a thorough overview of these and other correction schemes. The supercell approach can make the DFT calculations expensive. Additionally, brute-force DFT calculations do not necessarily explain why some materials favor and others disfavor V_o formation. Therefore, there is a need for efficient methods of calculating E_v —especially for metal oxides with disordered sublattices—using, e.g., phenomenological model

building and machine learning; we will survey such methods in the subsection Enthalpy Engineering in the section Materials Design Directions.

1.2.2 Standard Entropy of Oxygen Vacancy Formation

The second goal calls for an approach to compute the various contributions to ΔS_v : the translational, rotational, and vibrational entropy of gas-phase O_2 (ΔS_g , where “g” means “gas”); the phonon entropy change of solid-phase $MO_{x-\delta}$ (ΔS_p , where “p” means “phonon”); the configurational entropy change upon cation sublattice reduction (ΔS_c , where “c” means “configurational”); and the electronic entropy change (ΔS_e , where “e” means “electronic”). Note that for the rest of the chapter we drop the $^\circ$ from ΔS_v° for simplicity but it and its contributions remain standard entropy changes. Given the complexity and cost associated with calculating ΔS_g from first principles, one typically takes its measured value (e.g., $\Delta S_g = 15.9 k_B$ per $\frac{1}{2}O_2$ at 1800 K and 1 bar) from standard databases, such as NIST-JANAF [142]. For lower temperatures (i.e., usually <1000 K), accurate approaches for calculating ΔS_p include the frozen phonon method and density functional perturbation theory [143], invoking the harmonic approximation [144]. Calculating ΔS_p for higher temperatures requires the use of techniques that capture phonon anharmonicities, such as molecular dynamics (MD) simulations based on fluctuation-dissipation theory [145–148].

Calculating ΔS_c can be approached in a few different ways. The first scheme uses ideal-solution-based models to describe the entropy associated with the disordered reduction of cation sublattices by neutral- V_O donated electrons. Per mole of cation sublattice, the ideal solution-phase configurational entropy is given by

$$\Delta S_c^{ideal} = -nR \sum_i x_i \ln x_i \quad (1.26)$$

where n is the number of moles, i is the component index, and x is the mole fraction. In the first-principles-based sublattice formalism recently developed by Sai Gautam *et al.* [145–148], the excess entropy not captured by the ideal solution contributions is expressed in terms of binary interaction parameters (L) as within the compound energy formalism [150, 151]. For a system of two sublattices (e.g., one cation and one anion) and two components on each sublattice (e.g., oxidized metal M_{ox} and reduced metal M_{red} on the cation sublattice, and O and V_O on the anion sublattice), one can write the excess entropy as

$$\begin{aligned}
\Delta S^{excess} &= -\Delta G^{excess} / T \\
&= y_{M_{ox}}^c y_{M_{red}}^c y_O^a L_{M_{ox}, M_{red}:O} \\
&\quad + y_{M_{ox}}^c y_{M_{red}}^c y_{V_O}^a L_{M_{ox}, M_{red}:V_O} \\
&\quad + y_{M_{ox}}^c y_O^a y_{V_O}^a L_{M_{ox}:O, V_O} + y_{M_{red}}^c y_O^a y_{V_O}^a L_{M_{red}:O, V_O}
\end{aligned} \tag{1.27}$$

where y_X^z is the site fraction of the species X on the z sublattice [c = cation; a = anion in Eq. (1.27)].

While precedence for such sublattice models accurately describing phase behavior does exist, configurational entropy does not always exhibit ideal behavior in multicomponent, multi-sublattice systems. One can directly evaluate deviations from ideal behavior by converting the grand canonical output of cluster expansion-based Monte Carlo simulations into canonical quantities [152];

$$\langle S \rangle = \frac{1}{T} \left(\langle E \rangle - \Phi - \sum_i \mu_i \langle n_i \rangle \right) \tag{1.28}$$

where $\langle E \rangle$ is the thermodynamically averaged energy, Φ is the grand potential obtained by thermodynamic integration along a fixed T or fixed chemical potential (μ) path, and n_i is the number of species i exchanged with the μ reservoir. The main challenge with such an approach is parameterizing an accurate cluster-expansion Hamiltonian, which can sometimes require hundreds of first-principles quantum calculations. Additionally, it does not explicitly consider the effect of lattice expansion and vibrations on configurational entropy [153]. Note that while analytic approaches do exist for the calculation of ΔS_v , e.g., the statistical-thermodynamic theory of Ling (which applies to high concentrations of point defects) [154], we will not discuss them here because their derivations are involved.

Finally, we must establish an approach for computing ΔS_e , i.e., the electronic entropy changes upon changing the filling of a particular electron shell (e.g., 4f). In the opposing crystal potential method of Zhou and Aberg [155], one obtains the constraining Lagrange multipliers that act as a cancellation potential against the crystal field and lead to a spherical d-electron distribution. Table 1.2 lists the magnitudes of these different kinds of entropy contributions.

Table 1.2 Magnitudes of the different kinds of entropy contributions. Exp and RA means experiment and redox-active, respectively.

Contribution	ΔS [k_B per $\frac{1}{2}\text{O}_2(\text{g})$ produced]	Reference
$\text{O}_2(\text{g})$	15.9	[16] (exp, $T = 1800$ K)
Phonon	2.5 (for $\text{CeO}_{1.97}$)	[144] (theory, $T > 298.15$ K)
Configurational	<u>Ideal*</u> 9.7 (for $\text{CeO}_{1.97}$) 10.1 (for $\text{ABO}_{2.97}$, one RA cation) 11.5 (for $\text{ABO}_{2.97}$, two RA cations, one e^- /cation) <u>Cluster-expansion-based Monte Carlo</u> 5.9 ($\Delta S_p + \Delta S_c$, for $\text{CeO}_{1.97}$)	[152] (theory, $T = 1480$ K)
Electronic	4.5 (Ce^{4+} Ce^{3+} , in $\text{CeO}_{1.97}$)	[156] (theory, $T = 1800$ K)
Total	26.1 (for $\text{CeO}_{1.97}$)	[157] (exp, independent of T)

1.2.3 Stability

Of equal importance to a material's thermochemical properties (E_v and ΔS_v) is its stability with respect to decomposition into other compounds with the same summed stoichiometry. One can calculate the stability of a material by computing the Gibbs free energies of the redox-active material and all relevant secondary phases and then using the convex hull construction to calculate the phase diagram [158, 159]. For an isothermal, isobaric, closed system, the appropriate thermodynamic potential is G , which one can express as follows

$$\begin{aligned}
 G(T, P, \{N_i\}) &= E(T, P, \{N_i\}) + PV(T, P, \{N_i\}) - TS(T, P, \{N_i\}) \\
 &\approx E(T, P, \{N_i\}) - TS(T, P, \{N_i\})
 \end{aligned}
 \tag{1.29}$$

where E is the system's internal energy, T is the temperature, S is the entropy, P is the pressure, V is the volume, and N_i is the number of atoms of species i . Note that if one performs static DFT calculations, then $T = 0$ K. Therefore, one must take additional steps to evaluate the stability of the redox-active materials at $T \neq 0$ K. These steps generally involve including the relevant sources of entropy for a particular phase, which for solids mostly are due to vibrations and for gases are due to vibrations, rotations, and translations.

As mentioned above, for temperatures not too much higher than 298.15 K, the harmonic approximation provides an accurate and efficient means to compute vibrational entropies. At the temperatures relevant for thermal reduction (e.g., near 2000 K), phonon anharmonicities must be considered, which requires computation of, e.g., phonon spectra from DFT-MD simulations, which can be quite expensive. Phase transitions, such as melting, are also relevant at thermal reduction temperatures. However, currently, the only approach to accurately determine the melting point involves—in the absence of comprehensively validated classical interatomic potentials—costly DFT-MD simulations of solid-liquid coexistence.

1.2.4 Structure

One often would like to replace partially one of the metal elements in a metal oxide with another metal element to tune E_v , ΔS_v , and the stability. Such random alloys are hard to model quantum mechanically because the system dimensions that lend themselves to DFT calculations are often too small to accommodate a structure that one may regard as random. In other words, the periodicity imposed by boundary conditions introduces spurious correlations that make the modeled system deviate from the solid solution. One sometimes can alleviate this problem using so-called special quasi-random structures (SQSs) [160–162]. Finding the SQS generally amounts to minimizing an objective function that quantifies the difference between the current structure's site occupations and that of the random alloy. One such objective function (Q) is

$$Q = \sum_{\alpha \in A} |\Gamma_{\alpha} - \Gamma_{\alpha}^{target}| - \omega \quad (1.30)$$

where α is a cluster (e.g., pairs and triples of atoms within a prescribed distance cutoff), A is the list of all considered cluster definitions, and Γ is a cluster vector, whose elements are the average correlation (e.g., the product of pseudo-spin site identifiers) for each α . One compares the cluster vector of the SQS (Γ) with that of the random alloy (Γ^{target}), where the sum of their element-wise absolute deviations describes how much they differ. The second term in Equation (1.30) controls the importance of the distribution of the cluster vector deviations, where ω is the radius of the largest pair cluster, such that all clusters with the same or smaller radii have $\Gamma_{\alpha} - \Gamma_{\alpha}^{target} = 0$. SQS cells are the best possible approximations to random

alloys because their cluster vectors closely resemble the cluster vectors of truly random alloys.

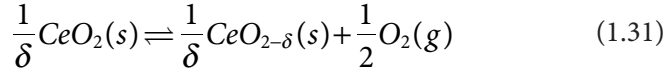
1.2.5 Kinetics

Finally, we note that kinetics can play an essential role in the efficiency of STWS cycles. From transition state theory, the critical kinetic parameter during thermal reduction is the activation energy of V_O diffusion ($E_{a,diff}$). For the water-splitting step, $E_{a,diff}$ again affects the kinetics though not as significantly as the activation energy of $H_2O(g)$ dissociation ($E_{a,diss}$). That said, some metal oxides dissociatively adsorb $H_2O(g)$ with no barrier [163–165], i.e., $E_{a,diss} = 0$. The activation energy typically is computed using a transition-state search algorithm, such as the nudged elastic band (NEB) method [166], which finds saddle points and minimum energy paths between predetermined reactants and products. The method works by optimizing several intermediate interpolated structures (images) along the reaction path. Each image finds the lowest energy possible while maintaining equal spacing to neighboring images. This constrained optimization is achieved by adding spring forces along the band between images and projecting out the forces' component due to the potential perpendicular to the band. In the original implementation of the NEB method, the highest energy image will not always be at a saddle point. The climbing image (CI) modification drives this image up to the nearest saddle point by removing its spring forces along the band [167, 168]. In this way, the image tries to maximize its energy along the band and minimize in all other directions. Other methods for finding the transition state include the modified single iteration synchronous-transit approach of Trottier *et al.* [169] and the modified CI-NEB approach of Caspersen and Carter [170], which, respectively, expedite the transition state search in solid-state reactions and extend the CI-NEB approach to solid-solid phase transitions that involve changes in the cell shape and volume. Once E_a 's are obtained, one can use them, along with pre-exponential factor estimates, in the construction of microkinetic models that determine the steady-state or time-evolving reaction yields as a function of, e.g., temperature, pressure, and the chemical potentials of the species in the system [171].

1.3 The State-of-the-Art Redox-Active Metal Oxide

To date, the most widely implemented off-stoichiometric metal oxide for STWS is $CeO_2(s)$ (ceria) [157, 172–185]. $CeO_2(s)$ is fluorite-structured and

crystallizes in the cubic $Fm\bar{3}m$ space group. Ce^{4+} bonds to eight equivalent O^{2-} atoms in a body-centered cubic geometry. Each O^{2-} bonds to four identical Ce^{4+} atoms to form a mixture of edge and corner-sharing OCe_4 tetrahedra. A favorable property of ceria is its ability to exchange oxygen via storing and releasing oxygen reversibly [186], i.e.,



Experimental findings show that ΔH_v varies with δ as

$$\Delta H_v(\delta) = b + m \log \delta = 4.09 - 0.33 \log \delta \quad (1.32)$$

where the intercept and slope are in eV [187]. Using a statistical thermodynamics model [187] of dilute defect clusters ($Ce^{3+}V_O Ce^{3+}$), Bulfin *et al.* derived the following equation of state for the equilibrium composition off-stoichiometric ceria:

$$\left(\frac{\delta}{\delta_m - \delta} \right)^{1/\delta_m} = \left(\frac{p_{O_2}}{p^o} \right)^{-1/2} \exp\left(\frac{\Delta S_g + \Delta S_p}{R} \right) \exp\left(-\frac{\Delta H_v(S)}{RT} \right) \quad (1.33)$$

Here, δ_m is the maximum oxygen off-stoichiometry (Appendix B. Equilibrium Composition of Ceria). Note that we are using the model of Bulfin *et al.* [187] and not the state-of-the-art thermodynamic model of Zinkevich [150] for pedagogical purposes as the former provides a simple, intuitive, and closed-form equation of state. At constant p_{O_2} , an increase in T leads to the reduction of $CeO_{2-\delta}(s)$, i.e., an increase in δ (Figure 1.6a). At constant T , a decrease in p_{O_2} also leads to an increase in δ . While thermal reduction of ceria typically requires temperatures around 1800 K, ceria exhibits excellent thermal stability with good resistance to sintering (which slows kinetics considerably) and a high melting point of 2670 K.

The main drawback of $CeO_2(s)$ is its too high $\Delta H_v = 4.4$ eV compared to the ideal range of 3.4 to 3.9 eV. Metal doping or substitution to decrease ΔH_v has been considered extensively. Ceria dopants/substitutions generally fall into five categories based on their valence: monovalent, divalent, trivalent, and multi-valent dopants, and tetravalent substitutions (Figure 1.6b). First, we will list some examples from these categories. Two monovalent dopants

studied are Li [188, 189] and K [190], where the former retains material porosity more effectively than pristine ceria [191]. Divalent dopants mostly have been sampled from the s-block alkaline earth metals—Mg [188, 192], Ca [188, 192, 193], Sr [188, 192, 193], and Ba [188]—though d-block Zn [194] also has been considered. Among the trivalent dopants studied, there are representative elements from the p block (Al [195]), d block (Sc [192, 194] and Y [192, 193, 196, 197]), and f block (La [196, 197], Sm [193, 197], Gd [193, 196, 197], and Dy [192]). While p-block elements, such as Si [79] and Sn [188], have been considered, the tetravalent d-block elements Zr [35, 110, 111, 191–193, 198–201] and Hf [191, 192] especially are promising, where the former is the most widely studied substitution. Experiments by Le Gal *et al.* show that the Ce^{4+} reduction yield ($y_{\text{Ce}^{3+}} \approx 2\delta$) increases linearly with Zr content (y_{Zr}) (Figure 1.6c) [196]. Therefore, Zr doping can be used to control the thermodynamics of V_O formation in ceria. Note that, even though Ti is directly above Zr in the periodic table, it softens samples at $T > 1700$ K, thereby limiting its use for STWS [191, 194]. Finally, multi-valent dopants have been examined as well, most of which are transition metals from the 3d block (V [194, 202], Cr [194, 203], Mn [178, 194], Fe [194, 204], Co [194], Ni [178, 194, 205], and Cu [178]), 4d block (Nb [79] and Rh [206]), and 5d block (Ta [175]); f-block Pr [191, 196] has been investigated too.

Now, we will develop an intuition for the relative effectiveness of Zr substitution compared to doping with other elements (Figure 1.6d) [38]. First, subvalent ($<4+$) doping decreases E_v [207] and increases δ [208, 209] to establish local charge neutrality. For example, the equilibrium composition of 10% Mg-doped ceria is $\text{Ce}_{0.9}\text{Mg}_{0.1}\text{O}_{1.9}$. Therefore, subvalent dopants decrease the number of reducible (i.e., fully coordinated) Ce^{4+} . Divalent transition-metal dopants also experience crystal field effects—e.g., the adoption of a square-planar coordination geometry—that increase the oxygen storage capacity of ceria [210]. Additionally, trivalent doping can affect the kinetics of V_O diffusion, where $E_{\text{a,diff}}$ correlates strongly with the ionic radius of the dopant [209]. Overall, aliovalent substitution does not improve significantly the Ce^{4+} reduction yield, $\text{O}_2(\text{g})$ released upon thermal reduction, or STWS efficiency.

For tetravalent substitutions, a long-held assumption was that Zr and Hf decrease E_v by compensating for ceria expansion upon reduction. However, Muhich and Steinfeld recently suggested that Zr and Hf dopants increase the δ of ceria because they store energy in tensile-strained Zr- or Hf-O bonds, which is released upon O-vacancy formation [207]. Here, we provide an alternative hypothesis: Zr and Hf weaken $\text{O}^{2-}\text{-Ce}^{4+}$ crystal bonds via bond order conservation [211]. To quantify crystal bond strength, we use the crystal bond dissociation energies (BDEs) developed by the authors [212]:

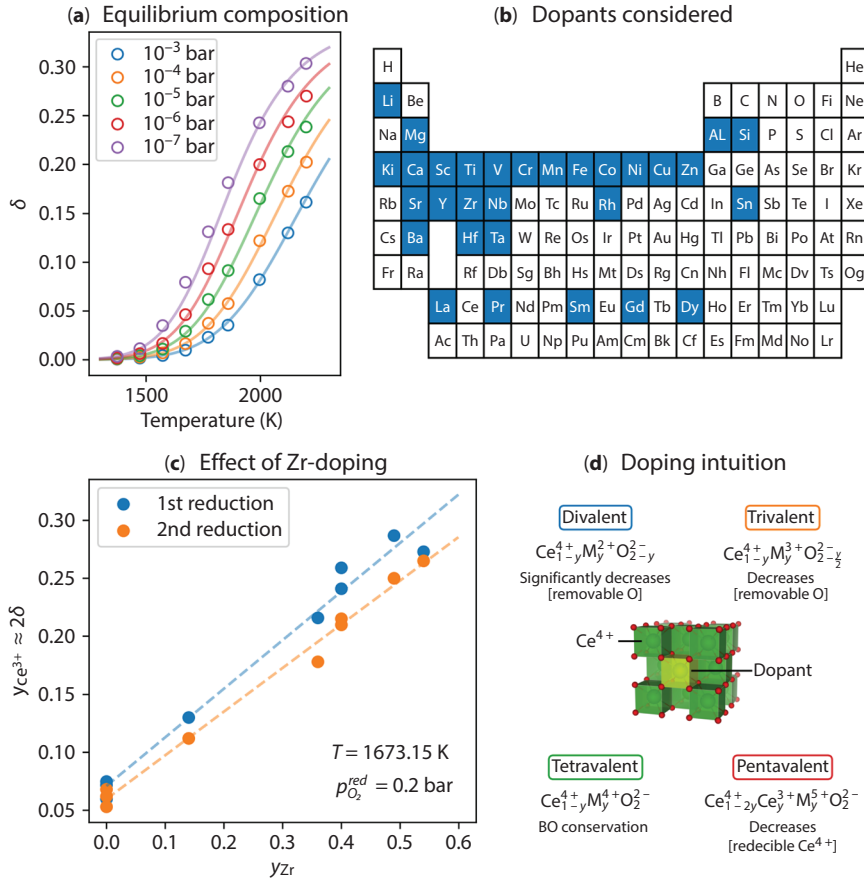


Figure 1.6 Ceria: the state-of-the-art STWS material. (a) Equilibrium composition of CeO_x as a function of temperature, showing the experimental data of Panlener *et al.* [157] and Dawicke and Blumenthal [213], (circles) and the kinetic model of Bulfin *et al.* [214] (lines, see Appendix B. Equilibrium Composition of Ceria). (b) Periodic table showing elements that have (blue) and have not (white) been considered as dopants or substitutions in ceria, based on the recent review by Bhosale *et al.* [174] (c) Percentage of Ce^{4+} reduced—which is $\approx 2\delta$ —during the first (blue) and second (orange) cycles of thermal reduction for STWS by ceria with different Zr doping concentrations [196]. (d) Summarizing the effect of dopant valence on properties critical to STWS yield [207]. “[x]” can be read as “the concentration of x.” For example, “[removable O]” means “the concentration of removable oxygen.”

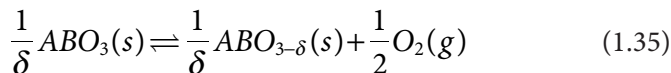
$$E_b[\text{O}^{2-} - \text{M}^{n+}] = \frac{-\Delta E_f[\text{MO}_{n/2}] + E_c[\text{M}] + (n/4)\text{BDE}[\text{O}_2]}{N_b[\text{O}^{2-} - \text{M}^{n+}]} \quad (1.34)$$

where n is the oxidation state of the metal (M) in the unreduced material, $\Delta E_f[\text{MO}_{n/2}]$ is the binary metal-oxide ($\text{MO}_{n/2}$) formation energy/enthalpy, $E_c[\text{M}]$ is the cohesive energy of the pure metal element, $\text{BDE}[\text{O}_2]$ is the bond dissociation energy of $\text{O}_2(\text{g})$ per atom, and $N_b[\text{O}^{2-} - \text{M}^{n+}]$ is the number of $\text{O}^{2-} - \text{M}^{n+}$ crystal bonds per $\text{MO}_{n/2}$ formula unit. For Ce^{4+} , Zr^{4+} , and Hf^{4+} , the experimental E_b is 2.56 eV, 3.27 eV, and 3.32 eV. Based on these crystal BDEs, O^{2-} forms stronger crystal bonds with Zr^{4+} and Hf^{4+} than Ce^{4+} . Therefore, Zr- and Hf-doping weaken $\text{O}^{2-} - \text{Ce}^{4+}$ crystal bonds on average, decreasing E_v and increasing δ . Despite the enthalpy control offered by Zr and Hf substitutions, the reoxidation thermodynamics of substituted ceria are not as favorable as for pure ceria [112, 149], which highlights a fundamental thermodynamic constraint in the design of metal oxides for thermochemical redox cycles: if reduction is made easier, then reoxidation necessarily is made harder [27, 110].

1.4 Next-Generation Perovskite Redox-Active Materials

Ceria remains the redox-active metal oxide of choice for STWS analysis, lab scale, and demonstration scale, and its undoped form provides the best thermodynamics. Therefore, ways to improve ceria properties are limited primarily to nonchemical changes, e.g., morphology engineering. Researchers more recently have explored more flexible materials classes like metal-oxide perovskites with the goal of designing superior materials. ABO_3 perovskites commonly crystallize in six lattice systems: cubic (e.g., $\text{Pm}\bar{3}\text{m}$ SrTiO_3), hexagonal (e.g., $\text{P6}_3/\text{mmc}$ SrMnO_3), rhombohedral (e.g., $\text{R}\bar{3}\text{c}$ LaCrO_3), tetragonal (e.g., P4mm BaTiO_3), orthorhombic (e.g., Pnma CaTiO_3), and monoclinic (e.g., $\text{P2}_1/\text{b}$ CeVO_3). The A- and B-site cations usually bond to O^{2-} in 12- and 6-coordinate geometry, respectively. The latter typically forms corner-sharing BO_6 octahedra but also can adopt edge- and face-sharing octahedra. Octahedra can take on tilt angles and patterns and exhibit Jahn-Teller distortion, thus demonstrating the diverse design degrees-of-freedom in the metal-oxide perovskite materials class.

Like ceria, redox-active ABO_3 perovskites can store and release oxygen reversibly



where $ABO_{3-\delta}$ is an off-stoichiometric, metal-oxide perovskite. Perovskites mostly fall under three categories: La-based perovskites, alkaline-earth-based perovskites, and layered, Ruddlesden-Popper perovskites. For La-based perovskites, La^{3+} occupies the A-site and a 3+ cation from either the p-block (e.g., Al^{3+} or Ga^{3+}) or d-block (e.g., Mn^{3+} or Fe^{3+}) resides on the B-site. The most widely investigated La-based perovskite composition is Sr-doped $LaMnO_3$ (LSM) [105, 215–217], which yields an estimated $\eta_{solar-to-fuel}$ lower (16%) than ceria (22%) at 1800 K but higher (13%) than ceria (7%) at 1600 K. The use of Al as a dopant in Sr-doped manganate aluminates $(Sr,La)(Mn,Al)O_3$ (Figure 1.7a) [218–220] enhances thermal reduction at 1623 K and has been shown to be stable for at least 80 cycles. Other A-site (Ca [221–223]) and B-site (Fe [216, 224] and Co [216]) substituents have been considered; however, LSM achieves the largest $H_2(g)$ production capacity. Recently, Chen *et al.* reported that Sr- and Co-doped $LaGaO_3$ produces more O_2 (at $T_{red} = 1623$ K and $p_{O_2}^{red} = 5 \times 10^{-6}$ bar) and H_2 (at $T_{ox} = 1073$ K and $\theta < 0.01$) per mass of redox-active material than LSM and ceria [225]. Reports of $H_2(g)$ production per mass of redox-active material, however, underscores one of the key problems the STWS field is trying to remedy: an apples-to-apples comparison between different perovskites (and ceria) currently is not possible from the literature reports. For example, lighter elements will automatically look better when higher productivities are reported in moles per redox-active material mass. That said, in the absence of apples-to-apples comparisons, the following lessons about Al-doped LSM can be learned: (1) Sr^{2+} -doping on the A-site produces Mn^{4+} , which is very reducible and therefore can be used to tune E_v , and (2) Al^{3+} -doping increases cycling stability because $LaAlO_3$ has a high melting temperature $T_m = 2350$ K.

For alkaline-earth-based perovskites, Ca^{2+} , Sr^{2+} , or Ba^{2+} reside on the A-site, and 4+ cations from the d-block occupy the B-site. Until recently, the most promising alkaline-earth-based perovskite oxide for STWS was $BaCe_{0.25}Mn_{0.75}O_3$ (BCM, Figure 1.7b) [226], which exhibits faster reoxidation kinetics than $Sr_{0.4}La_{0.6}Mn_{0.6}Al_{0.4}O_3$ and yields $2.5\times$ more $H_2(g)$ per atom than ceria when reduced at 1623 K. Note that these conditions correspond to lower $\eta_{solar-to-fuel}$ than at the target $T_{red} = 1723$ K from the second law of thermodynamics; the ideal scenario is to design a redox-active, metal-oxide perovskite that outperforms ceria at ≈ 1800 K. That said, BCM shows that one can use compositional engineering (i.e., with Ce^{4+} and Mn^{4+} cations on the B-site) to tune the thermodynamics (i.e., E_v) of metal-oxide

perovskites. Other ABO_3 perovskites—like $SrTi_{0.5}Mn_{0.5}O_3$ (STM) [227]—have been proposed; however, STM provides an E_v that is too low (≈ 2 - 2.5 eV vs. the ideal range of 3.4-3.9 eV) for maximally efficient water splitting. Recently, Sai Gautam *et al.* evaluated the E_v and thermodynamic stability of $Ca_{1-x}Ce_xMO_3$ perovskites, where $x = \{0, 0.5, 1\}$ and $M = \{Sc, Ti, V, Cr, Mn, Fe, Co, \text{ and } Ni\}$ (Figure 1.7c) [228]. $Ca_{0.5}Ce_{0.5}MnO_3$ (CCM) was identified to be a promising candidate, based on its favorable predicted $E_v = 3.65$ - 3.96 eV (range for symmetry-distinct $V_{O,S}$), which is similar to BCM in that Mn^{4+} is redox-active but is dissimilar in that in CCM, Ce^{4+} is redox-active and on the A-site. Interestingly, Sai Gautam *et al.* pointed out that the reduction of both the A- and B-sites should give additional configurational degrees of freedom to increase the ΔS_v of CCM, rather than if only one cation is redox-active. While CCM is thermodynamically (meta)stable, with an $E_{hull} = 39$ meV/atom, experimentally it fails to cycle. We recently postulated and validated that Ti-doping increases its stability, enables cycling, and does not degrade its attractive thermodynamic properties (E_v and ΔS_v) for STWS [229]. While the field of metal-oxide perovskites for STWS is fairly young—i.e., about one decade’s worth of research—the early returns have yielded some promising candidates (BCM and CCTM), and vast regions of materials design space remain unexplored, such as postquaternary compositions [early examples include $(Ba,Sr)(Co,Fe)O_3$ [216], Ce-doped $(Ba,Sr)MnO_3$ [230], and $(Y,Ca,Sr)MnO_3$ [231]] and layered structures [e.g., $(Ce,Sr)MnO_4$] [232, 233].

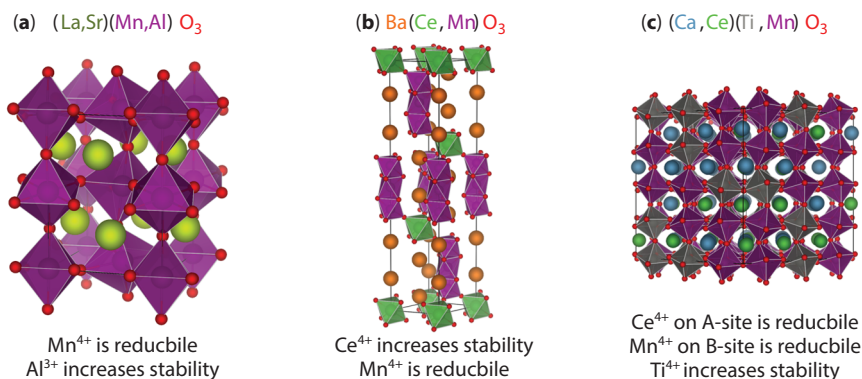


Figure 1.7 Promising perovskite metal oxides for STWS and the beneficial properties of the cations that comprise them.

1.5 Materials Design Directions

At this point, it is helpful to summarize what we know about the design of off-stoichiometric metal oxides for STWS. First, we know that the competing thermodynamics of thermal reduction and water splitting dictates a compromise (not too high and not too low) $\Delta H_v \approx E_v$ in the range of 3.4 to 3.9 eV, whereas ceria offers $E_v \approx 4.4$ eV [98]. Second, we know that configurational entropy is the most tunable contribution to ΔS_v , where cerium offers both ion/defect-disorder and electronic contributions. Third, we understand that the metal oxide must be the most stable compound at its composition and melt at temperatures well over 2000 K, where ceria does not form secondary phases upon thermal reduction and melts at 2670 K. Finally, we know that STWS kinetics should be fast; however, kinetics are usually fast for V_O diffusion and water splitting in off-stoichiometric/MIEC metal oxides compared to the kinetics of stoichiometric (line compounds) redox-active materials that undergo phase changes upon reduction and reoxidation [179]. We will not consider kinetics further here, but it certainly is important to consider in terms of the cycle times (longer cycle times will have a large impact on the economics) once satisfying the thermodynamic constraints.

1.5.1 Enthalpy Engineering

To design off-stoichiometric metal oxides with greater promise than ceria, one must identify materials with a lower $\Delta H_v \approx E_v$, between 3.4 and 3.9 eV. There are two main approaches: (1) high-throughput computational screening of E_v [108, 234–236] and (2) the development of electronic structure and thermodynamic descriptors for E_v . For example, Emery *et al.* took the first approach, calculating E_v using spin-polarized PBE+ U for more than 11,000 ternary metal-oxide perovskites in cubic and distorted crystal systems containing s-, p-, d-, and f-block metals on the A- and B-sites [236]. While that work has yet to identify any suitable (meeting multiple criteria) redox-active materials for STWS, it provides a valuable data set for future analysis of E_v and stability trends in perovskites.

In contrast, the second approach offers physical intuition for E_v that one can use to minimize both the number and cost of calculations required for materials discovery. One of the first electronic descriptors proposed for E_v was partial charges [120, 237]. In 2014, Michalsky *et al.* showed that E_v correlates positively ($R^2 \approx 0.63$) with the partial charge on the metal atom for a diverse collection of metal-oxide surfaces [120]. The logic here would

be that the more positive the partial charge on the metal atom, the stronger its electrostatic attraction to O^{2-} would be and, therefore, the higher its E_v should be. One year later, Ezbiri *et al.* found an even stronger correlation between E_v and the partial charge on the oxygen atom for several ABO_3 perovskites [237]. Here, one can apply the same logic as for the metal partial charges, *mutatis mutandis*.

That same year, Deml *et al.* published a phenomenological model for the E_v of 45 main-group and transition-metal oxides, covering a range of compositions and crystal structures. Their model approximates E_v as

$$E_v = 0.72 \left[0.60 \left(E_{Op} + \frac{3}{4} E_g + 2.60 \langle \Delta\chi \rangle \right) + |\Delta H_f| \right] - 2.07 \quad (1.36)$$

E_{Op} is the energy difference between the valence band maximum and the O 2p band center, E_g is the PBE+ U bandgap, $\langle \Delta\chi \rangle$ is the average Pauling electronegativity difference between O and its nearest metal neighbors, and ΔH_f is the formation enthalpy of the metal oxide [238]. This model introduces two new electronic descriptors— E_{Op} and E_g . E_{Op} relates to the oxygen partial charge because the greater the energy difference between the valence band maximum and the center of the O 2p band, the greater the occupation of the O 2p band and the more negative the partial charge on O; for this reason, E_v correlates positively with E_{Op} . In contrast, E_g includes the effect of electron (de)localization, where smaller and larger E_g correspond to greater delocalization and localization, respectively. When a neutral V_O forms, the departing oxygen leaves behind two electrons that reduce the lattice. If E_g is small, those electrons donate to metallic-like, delocalized bands that manifest in spatial delocalization over multiple ions, which stabilizes the V_O , corresponding to lower E_v s [239]. Conversely, if E_g is large, then those donated electrons localize on neighboring cations in high-energy conduction-band states, which destabilizes V_O . Therefore, larger E_g s correspond to higher E_v s, thereby explaining the positive correlation between E_v and E_g for both large and small band gap materials.

The model of Deml *et al.* also introduces two thermodynamic descriptors, $\langle \Delta\chi \rangle$ and ΔH_f . Whereas $\langle \Delta\chi \rangle$ ostensibly could correlate with BDEs of neutral metal-oxygen diatomic molecules [240], ΔH_f captures—albeit indirectly—the metal-oxygen bond strength in crystals and the effect of bulk stability on E_v [120, 241]. The orange data in Figure 1.8a shows the predictive capability of this model, as the PBE+ U -calculated and model-predicted E_v are in excellent agreement with only two outliers. While it is unclear why the $\langle \Delta\chi \rangle$ and ΔH_f proportions are $0.72 \cdot 0.60 \cdot 2.60 = 1.87$ [products of the coefficients

for $\langle \Delta\chi \rangle$ in Equation (1.36)] and 0.72, respectively, Deml *et al.* suggest that the combination of E_{Op} and E_g estimates the energy to donate V_O -generated electrons from the O 2p band to defect states in the gap. Recently, we developed crystal features analogous to gas-phase BDEs and standard reduction potentials, namely crystal BDEs [E_b , Equation (1.34)] and crystal reduction potentials [212], which we define as

$$V_r[M^{n+} \rightarrow M^{m+}] = -E_r[M^{n+} \rightarrow M^{m+}]/(n - m)F \quad (1.37)$$

where n and m are the oxidation states of the oxidized and reduced metals in the ground-state polymorphs of their binary metal-oxide crystals $MO_{n/2}(s)$ and $MO_{m/2}(s)$, respectively, F is the Faraday constant, and E_r is the (free) energy change of $MO_{n/2}(s)$ reduction to $MO_{m/2}(s)$ and $(n-m)/4 O_2(g)$. Subsequently, we constructed a thermodynamic model in the spirit of Hess' Law and Born-Haber cycles using E_b , V_r , E_g , and the energy above the convex hull E_{hull} . Our model for Deml *et al.*'s data (where we computed V_r and E_g from PBE+ U data [242, 243] on their set of crystals) is

$$E_v = -1.2 \max_{NN} V_r + 0.3E_g + 1.87 \text{ eV} \quad (1.38)$$

where we choose the maximum V_r value among the nearest-neighbor (NN) cations of a specific V_O , emphasizing the essential role of V_r in controlling E_v , seeing that it is one of only two features needed to attain excellent agreement between the PBE+ U -calculated and model-predicted E_v (blue data in Figure 1.8a). Our results also show that the presence of V_r in the model eliminates the two outliers. Additionally, $-c_r = 1.2$ has a physical interpretation as the number of electrons donated by a specific O^{2-} to its most reducible, nearest-cation neighbors upon V_O formation in a polar-covalent metal oxide.

We also built a state-of-the-art database of 341 SCAN+ U E_v s in ternary metal-oxide perovskites for an assortment of A-site (Ca, Sr, Ba, La, and Ce) and B-site (Ti, V, Cr, Mn, Fe, Co, and Ni) cations, crystal systems (cubic, tetragonal, orthorhombic, hexagonal, rhombohedral, and monoclinic), and diverse electronic structures, from insulators to metals. Our model for room-temperature-stable ($E_{hull} \leq 298.15 k_B$) ABO_3 perovskite structures is

$$E_v = 0.1 \sum_{NN} E_b - 1.5 \max_{NN} V_r + 0.4E_g - 55.8E_{hull} + 0.4 \text{ eV} \quad (1.39)$$

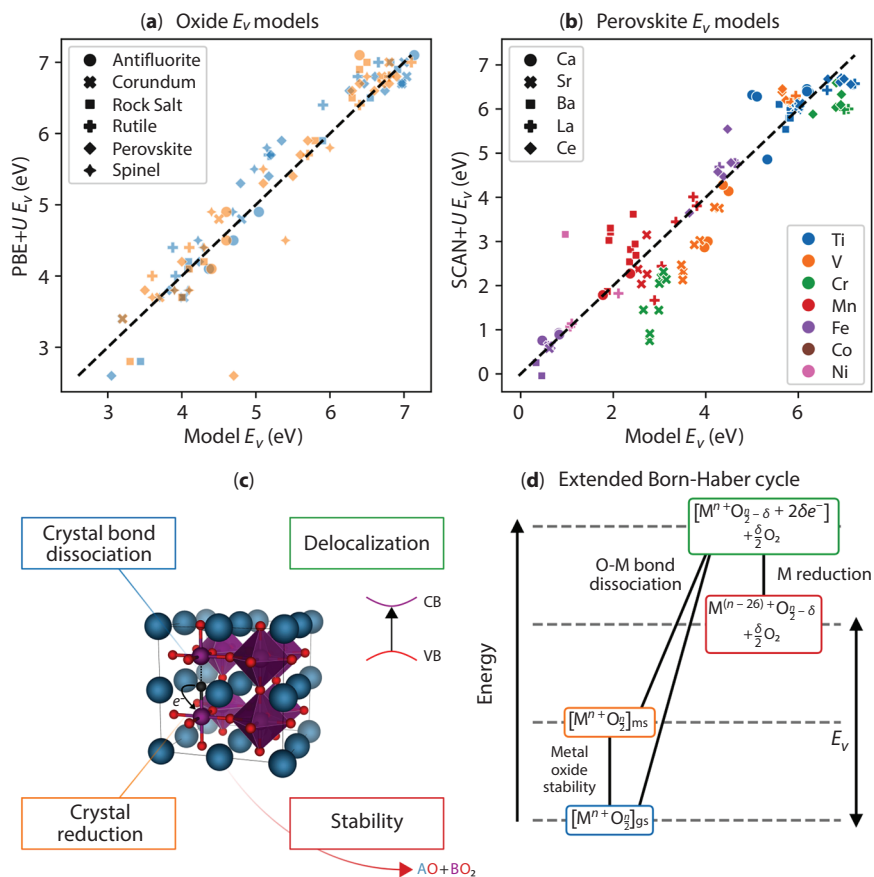


Figure 1.8 Materials enthalpy design directions for STWS metal oxides. E_v models for (a) six classes of oxides and (b) perovskite oxides. In panel (a), blue and orange correspond to the models in refs [212] and [238]. The former is based on crystal bond dissociation energies, crystal reduction potentials, band gaps, and energies above the convex hull. The latter is based on formation enthalpies, O 2p band centers, band gaps, and Pauling electronegativities averaged over the nearest neighbors of the V_O . Panel (b) shows the performance of the blue model in panel (a). Dashed diagonal lines in panels (a) and (b) correspond to lines of perfect agreement of DFT+ U and the model. An annotated structure that summarizes the contributions to E_v is shown in panel (c). Panel (d) depicts V_O formation as an extended Born-Haber cycle with three steps: metal-oxide destabilization (if the metal oxide is not in its ground-state polymorph), O-M crystal bond dissociation, and solid-state M reduction.

where the sum in the E_b term is over the NNs to the V_O . Figure 1.8b shows that Equation (1.39) accurately reproduces SCAN+ U E_v s for a diverse collection of metal-oxide perovskite compositions, with four intuitive terms that describe different energy contributions to E_v (Figure 1.8c). E_b is the energy to break O-M crystal bonds; interestingly, its coefficient of 0.1 suggests that V_O formation decreases the local bond order by only 10%. V_r is the energy to reduce the V_O 's neighboring cations, where its coefficient suggests that 1.5 of the V_O -generated electrons localize on neighboring cations. We interpret E_g as the energy associated with the donated electrons' (de)localization. The sum of the V_r and E_g coefficients is 1.9, indicating that, of the two ($1.9 \approx 2$) electrons left behind by a neutral V_O , on average 75% localize on neighboring cations while the other 25% delocalize. Finally, E_{hull} is the energy associated with metastability, and its significant coefficient is the result of small E_{hull} values (≤ 0.025 eV/atom) for room-temperature-stable ABO_3 perovskites. One can cast this intuition into a familiar form for a generic metal oxide: a modified Born-Haber cycle (Figure 1.8d). First, the energy increases by the metastability of the metal oxide, followed by an energy increase associated with O-M crystal bond dissociation. Depending on the cations' reducibility, the final step—cation reduction—can lead either to a decrease or an increase in the energy. The difference between the energy of the first and last step gives E_v .

Based on these insights, one can categorize the task of enthalpy engineering into four subtasks: to control crystal bond strength, crystal reducibility, electron (de)localization, and crystal stability concurrently to acquire a $\Delta H_v \approx E_v$ between 3.4 and 3.9 eV. For materials stable at 0 K, $E_{hull} = 0$; therefore, enthalpy engineering only involves three degrees of freedom. Fortunately, E_b and V_r are calculable, and E_g is available from existing measurements, which should help the field—experimentalists and theorists alike—to screen for stable metal-oxide materials with values of these features that satisfy the optimality constraints for E_v .

1.5.2 Entropy Engineering

The second direction in the design of off-stoichiometric metal oxides beyond ceria is to discover materials classes with tunable ΔS_v . As mentioned above, there are four main contributions to ΔS_v . First is the entropy of $\frac{1}{2}O_2(g)$ translations, rotations, vibrations, and electronic degrees of freedom, $\Delta S_g (= 15.9 k_B$ at 1800 K and $p_{O_2}^{red} = 1$ bar [142], where the standard pressure is chosen for convenience and the practical maximum is 0.2 bar, i.e., O_2 in air, and lower than ambient p_{O_2} s are desirable to increase the entropic driving force). However, ΔS_g cannot be engineered in such a way

that it benefits one redox-active material over another [244]. Second is the vibrational entropy change, ΔS_p (“p” means phonons), which—e.g., for the thermal reduction step of STWS—can be written in terms of the change in vibrational entropy with a change in the oxygen off-stoichiometry as

$$\Delta S_p = \frac{\partial S_p[MO_{x-\delta}]}{\partial \delta} \quad (1.40)$$

Here, MO_x can be either an off-stoichiometric or stoichiometric metal oxide. For off-stoichiometric metal oxides, ΔS_p is small ($2.5 k_B$ [144] for $CeO_{1.97}$) because V_O formation, except at high concentrations, has a modest impact on the low-energy phonon modes that control S_p . Therefore, for ceria and metal-oxide perovskites, ΔS_p is difficult to engineer to shift its status as the smallest contribution to ΔS_v . Certainly, ΔS_p can be larger for solar thermochemical cycles with stoichiometric materials due to solid-state phase changes (with attendant crystal composition, bonding, coordination, and lattice changes). However, materials that undergo major cation rearrangements upon reduction typically present kinetics and durability problems that may prevent their practical implementation.

The third contribution to ΔS_v is the entropy associated with a change in the number of unique electronic microstates, ΔS_e [133]. To illustrate where ΔS_e comes from, consider the example of the reduction of Ce^{4+} to Ce^{3+} in ceria, where the empty 4f shell of eight-fold-coordinated Ce^{4+} becomes singly occupied (Figure 1.9a) [156, 244]. In the absence of spin-orbit coupling (SOC) and crystal-field splitting (CFS), the 4f states of Ce are degenerate, which, using Boltzmann’s entropy formula, gives

$$\begin{aligned} \Delta S_e &= S_e[Ce^{3+}] - S_e[Ce^{4+}] = S_e[Ce^{3+}] = -k_B \sum_{i=1}^{14} p_i \ln p_i \quad (1.41) \\ &= k_B \ln 14 \approx 2.64 k_B \end{aligned}$$

where $p_i = 1/14$ is the probability of the electron occupying the i^{th} 4f state. Per V_O , $\Delta S_e = 5.28 k_B$ because V_O formation reduces two Ce^{4+} to Ce^{3+} . In the presence of SOC, the degenerate 4f states split into ${}^2F_{5/2}$ and ${}^2F_{7/2}$ levels, with a measured separation of ≈ 0.28 eV [245, 246] that leads to $\Delta S_e \approx 4.63 k_B$ per V_O at 1800 K. Clearly, SOC decreases ΔS_e by penalizing—via the Boltzmann distribution—microstates in which the electron occupies the higher energy levels. In the presence of both SOC and CFS, the ${}^2F_{5/2}$

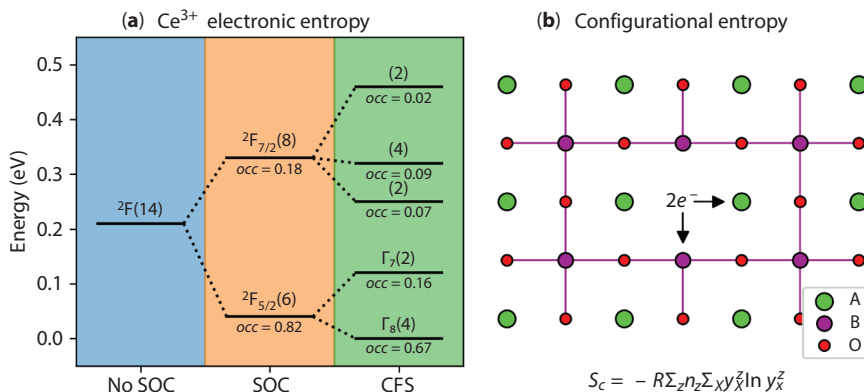


Figure 1.9 Directions for augmenting the (a) electronic and (b) configurational entropy upon V_O formation in the thermal reduction step of STWS. Panel (a) shows that, for ceria, eight-fold-coordinated Ce³⁺ in a cubic crystal field has many thermally accessible 4f states (number of microstates shown in parentheses), leading to a significant on-site electronic entropy change upon the reduction of Ce⁴⁺ (which has one possible configuration). SOC is spin-orbit coupling; CFS is crystal-field splitting; *occ* is the occupation of the state at 1800 K. Panel (b) illustrates the possibility of simultaneous reduction of both the A- and B-site cations, which increases the configuration entropy of the two reducing electrons left behind by a neutral V_O.

and ²F_{7/2} levels further split into five energy levels, as shown in the green panel of Figure 1.9a, which further reduces modestly ΔS_e to ≈4.48 k_B. Since energy-level degeneracy lifting only leads to a slight decrease in ΔS_e (0.80 k_B for Ce⁴⁺/Ce³⁺ at 1800 K), one can estimate its value from measurements of atomic spectra [245]. Incidentally, Naghavi *et al.* found that while S_e is sizable in all lanthanides, ΔS_e reaches a maximum value for Ce⁴⁺/Ce³⁺ reduction. Therefore, the take-home message is that to increase ΔS_e for off-stoichiometric metal oxides other than pristine ceria, one should dope or substitute with Ce⁴⁺ such that Ce⁴⁺ is redox-active (e.g., in CCTM but not BCM), E_v is optimal, and stability against decomposition and melting is maintained.

The fourth and final contribution to ΔS_v is the configurational entropy, ΔS_c, accompanying ion and defect disorder [152]. In other words, V_O formation creates oxidized/reduced metal disorder on the redox-active cation sublattices and O/V_O disorder on the anion sublattice that both contribute entropy to ΔS_v. For simplicity in discussing the engineerability of ΔS_c, we assume that all ion/defect configurations are equally likely, i.e., we can

describe the disorder as an ideal solution. For $\text{CeO}_{2-\delta}(\text{s})$, the mathematical expressions for S_c for both the cation and anion sublattices are given by

$$\text{Cation} \quad S_{c,\text{cation}} = -k_B [(1 - 2\delta) \ln(1 - 2\delta) + 2\delta \ln(2\delta)] \quad (1.42)$$

$$\text{Anion} \quad S_{c,\text{anion}} = -2k_B \left[\left(1 - \frac{\delta}{2}\right) \ln\left(1 - \frac{\delta}{2}\right) + \frac{\delta}{2} \ln \frac{\delta}{2} \right] \quad (1.43)$$

where $(1 - 2\delta)$ is the fraction of Ce^{4+} , 2δ is the fraction of Ce^{3+} , $1 - \delta/2$ is the fraction of O^{2-} , $\delta/2$ is the fraction of neutral V_O , and the “2” before k_B is the number of moles of O^{2-} per formula unit of pristine ceria. To compare against measurements, one calculates ΔS_c in the limit of an infinitesimal change in δ at the off-stoichiometry achieved, i.e., by taking the derivative of the sum of Equations (1.42) and (1.43) with respect to δ :

$$\Delta S_c(\delta) = \frac{\partial(S_{c,\text{cation}} + S_{c,\text{anion}})}{\partial\delta} = -k_B \left[2 \ln\left(\frac{2\delta}{1-2\delta}\right) + \ln\left(\frac{\delta}{2-\delta}\right) \right] \quad (1.44)$$

For $\delta = 0.03$ (i.e., $\text{CeO}_{1.97}$), $\Delta S_c = 9.7 k_B$, which is approximately two times larger than ΔS_e and four times larger than ΔS_p . V_O s in ceria have short-range order [247] and consequently, the real ΔS_c is nonideal and less than the ideal solution model [152].

Despite this reduction for real ion/defect solutions, ΔS_c still is the second-largest contribution to ΔS_v , and hence its modulation is a vital redox-active, metal-oxide engineering consideration. ΔS_c modulation is significant for $\text{ABO}_{3-\delta}$ perovskites. They commonly contain only one redox-active cation (ordinarily the B-site cation), resulting in configurational entropies per atom less than ceria for all δ/n , where n is the number of atoms in the formula unit (i.e., $n = 3$ for ceria and $n = 5$ for metal-oxide perovskites). Recently, we predicted theoretically that metal-oxide perovskites comprising two redox-active cations (e.g., Ce^{4+} and Mn^{4+}) exhibit a larger ΔS_c than those that undergo single cation reduction [228]. For $\text{ABO}_{3-\delta}(\text{s})$ that experience simultaneous cation reduction, the mathematical expression for $S_{c,\text{cation}}$ is

$$S_{c,\text{cation}} = -2k_B [(1 - \delta) \ln(1 - \delta) + \delta \ln \delta] \quad (1.45)$$

For simplicity, we suppose that the two V_o -generated electrons reduce the A- and B-site cations to the same degree. In the limit of $\Delta\delta \rightarrow 0$, ΔS_c for metal-oxide perovskites with simultaneous cation reduction is derived from the derivative of the sum of Equations (1.43) and (1.45) with respect to δ :

$$\Delta S_c(\delta) = -k_B \left[2 \ln \left(\frac{\delta}{1-\delta} \right) + \ln \left(\frac{\delta}{3-\delta} \right) \right] \quad (1.46)$$

For $ABO_{2.97}$ (i.e., $\delta = 0.03$), $\Delta S_c = 11.5 k_B/5 \text{ atoms} = 2.3 k_B/\text{atom}$, which is $0.9 k_B$ smaller than that of $CeO_{1.97}$ ($9.7 k_B/3 \text{ atoms} = 3.2 k_B/\text{atom}$). This simple analysis indicates that metal-oxide perovskites cannot produce ΔS_c per atom greater than ceria. Therefore, while identifying oxide materials classes that offer the possibility of simultaneous cation reduction enables entropy engineering, the key design direction for non-ceria STWS metal oxides is optimizing E_v (unless multiple redox can be realized in doped ceria).

1.5.3 Stability Engineering

We will briefly mention a third materials design direction: to engineer the stability of off-stoichiometric metal oxides. Such engineering, however, requires a better atomic-scale understanding of temperature-dependent phase diagrams and melting points (T_m) of materials. At temperatures where the harmonic approximation breaks down, which are relevant in STWS, one must either include the anharmonic force constants in evaluating the vibrational free energy or perform MD simulations using the fluctuation-dissipation theorem to capture anharmonic contributions crucial in controlling phase-transition temperatures. An alternative approach to account for anharmonicities is the utilization of enhanced sampling (e.g., nested sampling), which allows for the direct calculation of the partition function (and hence thermodynamic properties) [248]. All three of these approaches are computationally challenging if one desires a quantum mechanical description of the material. Therefore, new methods, such as machine-learned potentials, are starting to be used to ease the computational burden of these calculations [249]. The modeling of material melting faces the same challenges, as—in the absence of an accurate analytic theory or phenomenology for T_m prediction—MD simulations of phase coexistence are necessary with either computationally expensive quantum mechanics techniques or more efficient machine-learned potentials.

However, the latter often require computationally demanding parameterization based on accurate quantum mechanics computations as well. That said, melting point measurements are available in the literature; therefore, instead of a materials design direction, we recommend a target for theoretical method development could be data-driven T_m prediction for multi-component solid solutions using the modern tools of data science and machine learning based on experimental data of simpler but related compounds.

1.6 Conclusions

Solar thermochemical water splitting could be a crucial component of a coordinated technological effort to mitigate the effects of climate change. The potential of thermochemical technologies based on concentrated solar radiation is exceptionally promising, given that they utilize the entire solar spectrum and can generate local temperatures that all but preclude kinetic limitations for crucial chemical reactions. Two-step solar-thermochemical water-splitting cycles typically use redox-active metal oxides that can be reversibly reduced and reoxidized over a large number of cycles. The most promising of these are off-stoichiometric/MIEC or oxygen-vacancy-forming metal oxides, such as ceria and redox-active perovskites—due to their unhindered kinetics and the latter’s large composition space. This chapter introduced the fundamentals of thermochemical water splitting at high temperatures, focusing on thermodynamics and discovery of off-stoichiometric metal oxides. We also provided a high-level overview of the computational methods available to calculate the various critical quantities controlling the efficiency of solar thermochemical water splitting cycles to produce hydrogen. Having surveyed important literature on ceria and redox-active metal-oxide perovskites, we closed with a forward-looking assessment addressing what avenues researchers might follow next in the pursuit of off-stoichiometric metal-oxide materials that could lead to widespread deployment of this technology.

Acknowledgments

The authors gratefully acknowledge research support from the HydroGEN Advanced Water Splitting Materials Consortium, established as part of the Energy Materials Network under the U.S. Department of Energy, Office of Energy Efficiency and Renewable Energy, Fuel Cell Technologies Office,

under Award Number DE-EE0008090. The authors also acknowledge the computational resources sponsored by the Department of Energy's Office of Energy Efficiency and Renewable Energy located at the National Renewable Energy Laboratory. The authors also thank Princeton University for computing resources. The views and opinions of the authors expressed herein do not necessarily state or reflect those of the United States Government or any agency thereof. Neither the United States Government nor any agency thereof, nor any of their employees, makes any warranty, expressed or implied, or assumes any legal liability or responsibility for the accuracy, completeness, or usefulness of any information, apparatus, product, or process disclosed, or represents that its use would not infringe privately owned rights.

Appendices

Appendix A. Equilibrium Composition for Solar Thermolysis

One can calculate the equilibrium composition of the gas-phase mixture present in solar thermolysis using the Gibbs-free-energy-minimization method, subject to system constraints, which starts with the definition of the partial molar Gibbs free energy

$$\frac{nG}{RT} = \sum_i n_i \left(\frac{\Delta G_{f,i}^{\circ}}{RT} + \ln y_i p \right) \quad (1.47)$$

where n is the total number of moles, G is the Gibbs free energy per mole of the mixture, R is the ideal gas constant, T is the temperature in K, n_i is the number of moles of component i , y_i is the mole fraction of component i , p is the pressure, and $\Delta G_{f,i}^{\circ}$ is the Gibbs free energy of formation of component i at standard conditions. $\Delta G_{f,i}^{\circ}$ can be obtained from online databases—such as the NIST-JANAF thermochemical tables—or reference books—e.g., Barin's Thermochemical Data of Pure Substances. Here, we use the Fact-Web application, which offers user-friendly access to the FactSage pure substances database, to download the $\Delta G_{f,i}^{\circ}$ of $\text{H}_2\text{O}(\text{g})$, $\text{H}_2(\text{g})$, $\text{O}_2(\text{g})$, $\text{H}(\text{g})$, $\text{O}(\text{g})$, and $\text{OH}(\text{g})$ at 1 bar and temperatures ranging from 200 K to 6000 K in increments of 100 K. The objective of the method above is to find the set of n_i that minimize the Gibbs free energy of the mixture

$$\min_{n_i} \frac{nG}{RT} \quad (1.48)$$

which, of course, is a requirement—enforced by the second law of thermodynamics—for a system at equilibrium, where the T and p are held constant. Additionally, for a closed system, we must apply an atomic balance constraint, namely

$$n_{H,in} = n_{H,out} \quad (1.49)$$

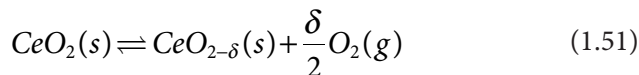
$$n_{O,in} = n_{O,out} \quad (1.50)$$

such that the number of moles (n) of H and O atoms in molecules fed to (*in*) and leaving (*out*) the reactor are equal.

To solve Equations (1.48)-(1.50), we used the Sequential Least-Squares Programming (SLSQP) method implemented in `scipy` [250] with a convergence threshold of 1×10^{-6} . We also placed boundaries on y_i such that—at equilibrium—they must acquire physically reasonable values between 0 and 1, inclusive. We reasonably assume that no $\text{H}_2\text{O}(g)$ dissociates at the lowest T . In other words, we set $n_{\text{H}_2\text{O}(g)} = 1$ and $n_{\text{H}_2(g)} = n_{\text{O}_2(g)} = n_{\text{H}(g)} = n_{\text{O}(g)} = n_{\text{OH}(g)} = 0$. For $T > \text{lowest } T$, we supplied the n_i from the previous (lower) T as an initial guess for the equilibrium composition. The Python code used to generate Figure 1.2b can be found at <https://github.com/wexlergroup/stws/> as a Jupyter notebook.

Appendix B. Equilibrium Composition of Ceria

One approach to computing the equilibrium composition of $\text{CeO}_2(s)$ as a function of T and p_{O_2} is to solve a set of kinetic equations under the steady-state approximation [214]. We use this semi-empirical model and not the state-of-the-art thermodynamic model of Zinkevich [150] as the former provides a simple, intuitive, and closed-form equation of state. One can write the thermal reduction of $\text{CeO}_2(s)$ as follows



where δ is the oxygen off-stoichiometry produced by oxygen vacancy (V_{O}) formation. The rate of change of the V_{O} concentration $[V_{\text{O}}]$ is the

difference between the rates of the forward and backward reactions [Equation (1.51)],

$$\frac{d[V_O]}{dt} = k_{red}[O] - k_{ox}[V_O]p_{O_2}^n \quad (1.52)$$

Here, k is a rate constant, *red* stands for reduction, *ox* stands for reoxidation, $[O]$ is the removable oxygen concentration, p_{O_2} is the partial pressure of $O_2(g)$, and n is the oxygen gas power dependency that depends on the maximum δ , which we denote as δ_m . Setting $d[V_O]/dt = 0$ at equilibrium and isolating the concentration terms, we obtain

$$\frac{[V_O]}{[O]} = \frac{k_{red}}{k_{ox}} P_{O_2}^{-n} = \frac{\delta}{\delta_m - \delta} \quad (1.53)$$

Note that we have rewritten the ratio of removed to removable O—i.e., $[V_O]/[O]$ —in terms of δ and δ_m . To introduce the energetics of V_O formation in our treatment, we assume an Arrhenius relationship between a reaction's rate and its activation barrier (E_a)

$$k = k_0 e^{-\frac{E_a}{RT}} \quad (1.54)$$

where k_0 is an empirical prefactor. Replacing k_{red} and k_{ox} with their associated Arrhenius rate expressions and labeling the difference between the E_a s for reduction and reoxidation as ΔE , we can rewrite Equation (1.53) as

$$\frac{\delta}{\delta_m - \delta} = \frac{k_{red,0}}{k_{ox,0}} P_{O_2}^{-n} e^{-\frac{\Delta E}{RT}} \quad (1.55)$$

which, upon solving for δ , yields

$$\delta = \frac{\delta_m}{\frac{k_{ox,0}}{k_{red,0}} P_{O_2}^n e^{\frac{\Delta E}{RT}} + 1} \quad (1.56)$$

In the original derivation of this model, Bulfin *et al.* fit Equation (1.56) to equilibrium measurements of ceria for the triplets (δ , T , p_{O_2}) and obtained $k_{\text{red},0}/k_{\text{ox},0} = 8700 \pm 800 \text{ bar}^n$, $n = 0.218 \pm 0.0013$, $\delta_m = 0.35$, and $\Delta E = 195.6 \pm 1.2 \text{ kJ/mol}$ [214]. Note that the V_O formation energy per $\frac{1}{2} \text{O}_2$ is $E_v = \Delta E/2n \approx 4.6 \text{ eV}$. The Python code used to generate Figure 1.6a can be found at <https://github.com/wexlergroup/stws/> as a Jupyter notebook.

References

1. *Climate Change 2014: Synthesis Report. Contribution of Working Groups I, II and III to the Fifth Assessment Report of the Intergovernmental Panel on Climate Change*, p. 151, IPCC Geneva, Switzerland, 2014, <https://www.ipcc.ch/report/ar5/syr/>.
2. *Global Climate Change Impacts in the United States: A State of Knowledge Report*, Cambridge University Press, New York, NY, 2009.
3. Oreskes, N., The scientific consensus on climate change. *Science*, 306, 1686–1686, 2004.
4. Steinfeld, A., Solar thermochemical production of hydrogen—A review. *Sol. Energy*, 78, 603–615, 2005.
5. Walter, M.G., Warren, E.L., McKone, J.R., Boettcher, S.W., Mi, Q., Santori, E.A., Lewis, N.S., Solar water splitting cells. *Chem. Rev.*, 110, 6446–6473, 2010.
6. Rajan, A.G., Martirez, J.M.P., Carter, E.A., Why do we use the materials and operating conditions we use for heterogeneous (photo) electrochemical water splitting? *ACS Catal.*, 10, 11177–11234, 2020.
7. Laguna-Bercero, M.A., Recent advances in high temperature electrolysis using solid oxide fuel cells: A review. *J. Power Sources*, 203, 4–16, 2012.
8. Ayers, K., Danilovic, N., Ouimet, R., Carmo, M., Pivovar, B., & Bornstein, M., Perspectives on low-temperature electrolysis and potential for renewable hydrogen at scale. *Annu. Rev. Chem. Biomol. Eng.*, 10, 219–239, 2019.
9. Zhao, Y., Dunn, A., Lin, J., Shi, D., *Novel Nanomaterials for Biomedical, Environmental and Energy Applications*, pp. 415–434, Elsevier, Amsterdam, Netherlands, 2019.
10. Schäppi, R., Rutz, D., Dähler, F., Muroyama, A., Haueter, P., Lilliestam, J., Patt, A., Furler, P., Steinfeld, A., Drop-in fuels from sunlight and air. *Nature*, 601, 63–68, 2022.
11. Zhou, E., Xu, K., Wang, C., *Analysis of the Cost and Value of Concentrating Solar Power in China*, National Renewable Energy Laboratory, Golden, CO, 2019, <https://www.nrel.gov/docs/fy20osti/74303.pdf>.
12. Fletcher, E.A., Solarthermal processing: A review. *J. Sol. Energy Eng.*, 123, 63–74, 2000.

13. Romero, M. and Steinfeld, A., Concentrating solar thermal power and thermochemical fuels. *Energy Environ. Sci.*, 5, 9234–9245, 2012.
14. Cheng, W.-H., de la Calle, A., Atwater, H.A., Stechel, E.B., Xiang, C., Hydrogen from sunlight and water: A side-by-side comparison between photoelectrochemical and solar thermochemical water-splitting. *ACS Energy Lett.*, 6, 3096–3113, 2021.
15. Fletcher, E.A. and Moen, R.L., Hydrogen and oxygen from water: The use of solar energy in a one-step effusional process is considered. *Science*, 197, 1050–1056, 1977.
16. Bale, C.W., Bélisle, E., Chartrand, P., Deckerov, S.A., Eriksson, G., Gheribi, A.E., Hack, K., Jung, I.-H., Kang, Y.-B., Melançon, J., Pelton, A.D., Petersen, S., Robelin, C., Sangster, J., Spencer, P., Van Ende, M.-A., FactSage thermochemical software and databases, 2010–2016. *Calphad*, 54, 35–53, 2016.
17. Steinfeld, A., Solar hydrogen production via a two-step water-splitting thermochemical cycle based on Zn/ZnO redox reactions. *Int. J. Hydrog. Energy*, 27, 611–619, 2002.
18. Pretzel, C.W. and Funk, J.E., *Developmental Status of Solar Thermochemical Hydrogen Production*, p. 114, Sandia Natl. Lab, Albuquerque, New Mexico, 1987.
19. Perret, R., *Solar Thermochemical Hydrogen Production Research (STCH)*, SAND2011–3622, 1219357, Sandia National Laboratories, Albuquerque, New Mexico, 2011.
20. Department of Energy (DOE), Office of Energy Efficiency and Renewable Energy (EERE), *Fuel Cell Technologies Office Annual FOA, Funding Opportunity Announcement (FOA) Number: DE-FOA-0001647*, Department of Energy, Washington, DC, 2016.
21. Rao, C.N.R. and Dey, S., Solar thermochemical splitting of water to generate hydrogen. *Proc. Natl. Acad. Sci.*, 114, 13385–13393, 2017.
22. Abanades, S., Charvin, P., Flamant, G., Neveu, P., Screening of water-splitting thermochemical cycles potentially attractive for hydrogen production by concentrated solar energy. *Energy*, 31, 2805–2822, 2006.
23. Perkins, C. and Weimer, A.W., Solar-thermal production of renewable hydrogen. *AIChE J.*, 55, 286–293, 2009.
24. Funk, J.E., Thermochemical hydrogen production: Past and present. *Int. J. Hydrog. Energy*, 26, 185–190, 2001.
25. Kodama, T. and Gokon, N., Thermochemical cycles for high-temperature solar hydrogen production. *Chem. Rev.*, 107, 4048–4077, 2007.
26. Muhich, C.L., Ehrhart, B.D., Al-Shankiti, I., Ward, B.J., Musgrave, C.B., Weimer, A.W., A review and perspective of efficient hydrogen generation via solar thermal water splitting: A review and perspective of efficient hydrogen generation. *Wiley Interdiscip. Rev. Energy Environ.*, 5, 261–287, 2016.
27. Miller, J.E., McDaniel, A.H., Allendorf, M.D., Considerations in the design of materials for solar-driven fuel production using metal-oxide thermochemical cycles. *Adv. Energy Mater.*, 4, 1300469, 2014.

28. Steinfeld, A., Kuhn, P., Reller, A., Palumbo, R., Murray, J., Tamaura, Y., Solar-processed metals as clean energy carriers and water-splitters. *Int. J. Hydrog. Energy*, 23, 767–774, 1998.
29. Zheng, Z., Liu, T., Liu, Q., Lei, J., Fang, J., A distributed energy system integrating SOFC-MGT with mid-and-low temperature solar thermochemical hydrogen fuel production. *Int. J. Hydrog. Energy*, 46, 19846–19860, 2021.
30. Budama, V.K., Johnson, N.G., McDaniel, A., Ermanoski, I., Stechel, E.B., Thermodynamic development and design of a concentrating solar thermochemical water-splitting process for co-production of hydrogen and electricity. *Int. J. Hydrog. Energy*, 43, 17574–17587, 2018.
31. Bilgen, E. and Bilgen, C., Solar hydrogen production using two-step thermochemical cycles. *Int. J. Hydrog. Energy*, 7, 637–644, 1982.
32. Kodama, T., High-temperature solar chemistry for converting solar heat to chemical fuels. *Prog. Energy Combust. Sci.*, 29, 567–597, 2003.
33. Scheffe, J.R. and Steinfeld, A., Oxygen exchange materials for solar thermochemical splitting of H_2O and CO_2 : A review. *Mater. Today*, 17, 341–348, 2014.
34. Funk, J.E. and Reinstrom, R.M., Energy requirements in production of hydrogen from water. *Ind. Eng. Chem. Process Des. Dev.*, 5, 336–342, 1966.
35. Loutzenhiser, P.G., Meier, A., Steinfeld, A., Review of the two-step H_2O/CO_2 -splitting solar thermochemical cycle based on Zn/ZnO redox reactions. *Materials*, 3, 4922–4938, 2010.
36. Stamatiou, A., Loutzenhiser, P.G., Steinfeld, A., Solar syngas production via H_2O/CO_2 -splitting thermochemical cycles with Zn/ZnO and FeO/Fe₃O₄ redox reactions. *Chem. Mater.*, 22, 851–859, 2010.
37. Stamatiou, A., Loutzenhiser, P.G., Steinfeld, A., Syngas production from H_2O and CO_2 over Zn particles in a packed-bed reactor. *AIChE J.*, 58, 625–631, 2012.
38. Abanades, S., Metal oxides applied to thermochemical water-splitting for hydrogen production using concentrated solar energy. *ChemEngineering*, 3, 63, 2019.
39. Palumbo, R., High temperature solar electrothermal processing—III. Zinc zinc Oxide at 1200–1675K using non-consumable anode. *Energy*, 13, 319–332, 1988.
40. Fletcher, E.A., Solarthermal and solar quasi-electrolytic processing and separations: Zinc from zinc oxide as an example. *Ind. Eng. Chem. Res.*, 38, 2275–2282, 1999.
41. Abanades, S., Charvin, P., Lemont, F., Flamant, G., Novel two-step SnO_2/SnO water-splitting cycle for solar thermochemical production of hydrogen. *Int. J. Hydrog. Energy*, 33, 6021–6030, 2008.
42. Charvin, P., Abanades, S., Lemont, F., Flamant, G., Experimental study of $SnO_2/SnO/Sn$ thermochemical systems for solar production of hydrogen. *AIChE J.*, 54, 2759–2767, 2008.

43. Levêque, G., Abanades, S., Jumas, J.-C., Olivier-Fourcade, J., Characterization of two-step tin-based redox system for thermochemical fuel production from solar-driven CO_2 and H_2O splitting cycle. *Ind. Eng. Chem. Res.*, 53, 5668–5677, 2014.
44. Scheffe, J.R., McDaniel, A.H., Allendorf, M.D., Weimer, A.W., Kinetics and mechanism of solar-thermochemical H_2 production by oxidation of a cobalt ferrite-zirconia composite. *Energy Environ. Sci.*, 6, 963–973, 2013.
45. Teknetzi, I., Nessi, P., Zaspalis, V., Nalbandian, L., Ni-ferrite with structural stability for solar thermochemical $\text{H}_2\text{O}/\text{CO}_2$ splitting. *Int. J. Hydrog. Energy*, 42, 26231–26242, 2017.
46. Lorentzou, S., Zygogianni, A., Pagkoura, C., Karagiannakis, G., Konstandopoulos, A.G., Saeck, J.P., Breuer, S., Lange, M., Lapp, J., Fend, T., Roeb, M., Gonzalez, A.J., Delgado, A.V., Brouwer, J.P., Makkus, R.C., Kiartzis, S.J., Hydrosol-plant: Structured redox reactors for H_2 production from solar thermochemical H_2O splitting. *AIP Conf. Proc.*, 2033, 130010, 2018.
47. Bhosale, R.R., Thermodynamic analysis of Ni-ferrite based solar thermochemical H_2O splitting cycle for H_2 production. *Int. J. Hydrog. Energy*, 44, 61–71, 2019.
48. Diver, R.B., Miller, J.E., Allendorf, M.D., Siegel, N.P., Hogan, R.E., Solar thermochemical water-splitting ferrite-cycle heat engines. *J. Sol. Energy Eng.*, 130, 041001, 2008.
49. Bhosale, R.R., Shende, R.V., Puszynski, J.A., Sol-gel derived NiFe_2O_4 modified with ZrO_2 for hydrogen generation from solar thermochemical water-splitting reaction. *MRS Online Proc. Libr.*, 1387, 5, 2011.
50. Allen, K.M., Coker, E.N., Auyeung, N., Klausner, J.F., Cobalt ferrite in YSZ for use as reactive material in solar thermochemical water and carbon dioxide splitting, part I: Material characterization. *JOM*, 65, 1670–1681, 2013.
51. Allen, K.M., Auyeung, N., Rahmatian, N., Klausner, J.F., Coker, E.N., Cobalt ferrite in YSZ for use as reactive material in solar thermochemical water and carbon dioxide splitting, part ii: Kinetic modeling. *JOM*, 65, 1682–1693, 2013.
52. Dimitrakis, D.A., Syrigou, M., Lorentzou, S., Kostoglou, M., Konstandopoulos, A.G., On kinetic modelling for solar redox thermochemical H_2O and CO_2 splitting over NiFe_2O_4 for H_2 , CO and syngas production. *Phys. Chem. Chem. Phys.*, 19, 26776–26786, 2017.
53. Bhosale, R.R., Mn-ferrite based solar thermochemical water splitting cycle: A thermodynamic evaluation. *Fuel*, 256, 115847, 2019.
54. Dimitrakis, D.A., Tsongidis, N., II, Konstandopoulos, A.G., Reduction enthalpy and charge distribution of substituted ferrites and doped ceria for thermochemical water and carbon dioxide splitting with DFT+U. *Phys. Chem. Chem. Phys.*, 18, 23587–95, 2016.
55. Gokon, N., Hasegawa, T., Takahashi, S., Kodama, T., Thermochemical two-step water-splitting for hydrogen production using Fe-YSZ particles and a ceramic foam device. *Energy*, 33, 1407–1416, 2008.

56. Gokon, N., Murayama, H., Umeda, J., Hatamachi, T., Kodama, T., Monoclinic zirconia-supported Fe₃O₄ for the two-step water-splitting thermochemical cycle at high thermal reduction temperatures of 1400–1600°C. *Int. J. Hydrog. Energy*, 34, 1208–1217, 2009.
57. Nakamura, T., Hydrogen production from water utilizing solar heat at high temperatures. *Sol. Energy*, 19, 467–475, 1977.
58. Charvin, P., Abanades, S., Flamant, G., Lemort, F., Two-step water splitting thermochemical cycle based on iron oxide redox pair for solar hydrogen production. *Energy*, 32, 1124–1133, 2007.
59. Steinfeld, A., Sanders, S., Palumbo, R., Design aspects of solar thermochemical engineering—a case study: Two-step water-splitting cycle using the Fe₃O₄/FeO redox system. *Sol. Energy*, 65, 43–53, 1999.
60. Allendorf, M.D., Diver, R.B., Siegel, N.P., Miller, J.E., Two-step water splitting using mixed-metal ferrites: Thermodynamic analysis and characterization of synthesized materials. *Energy Fuels*, 22, 4115–4124, 2008.
61. Tamaura, Y., Steinfeld, A., Kuhn, P., Ehrensberger, K., Production of solar hydrogen by a novel, 2-step, water-splitting thermochemical cycle. *Energy*, 20, 325–330, 1995.
62. Kodama, T., Kondoh, Y., Yamamoto, R., Andou, H., Satou, N., Thermochemical hydrogen production by a redox system of ZrO₂-supported Co (II)-ferrite. *Sol. Energy*, 78, 623–631, 2005.
63. Bulfin, B., Vieten, J., Agrafiotis, C., Roeb, M., Sattler, C., Applications and limitations of two step metal oxide thermochemical redox cycles: A review. *J. Mater. Chem. A*, 5, 18951–18966, 2017.
64. Tamaura, Y., Kojima, M., Sano, T., Ueda, Y., Hasegawa, N., Tsuji, M., Thermodynamic evaluation of water splitting by a cation-excessive (Ni, Mn) ferrite. *Int. J. Hydrog. Energy*, 23, 1185–1191, 1998.
65. Tamaura, Y., Ueda, Y., Matsunami, J., Hasegawa, N., Nezuka, M., Sano, T., Tsuji, M., Solar hydrogen production by using ferrites. *Sol. Energy*, 65, 55–57, 1999.
66. Ohlhausen, J.A.T., Coker, E.N., Ambrosini, A., Miller, J.E., ToF-SIMS analysis of iron oxide particle oxidation by isotopic and multivariate analysis: ToF-SIMS of FeO_x particle oxidation by isotopic and multivariate. *Surf. Interface Anal.*, 45, 320–323, 2013.
67. Kodama, T., Gokon, N., Yamamoto, R., Thermochemical two-step water splitting by ZrO₂-supported Ni_xFe_{3-x}O₄ for solar hydrogen production. *Sol. Energy*, 82, 73–79, 2008.
68. Gokon, N., Murayama, H., Nagasaki, A., Kodama, T., Thermochemical two-step water splitting cycles by monoclinic ZrO₂-supported NiFe₂O₄ and Fe₃O₄ powders and ceramic foam devices. *Sol. Energy*, 83, 527–537, 2009.
69. Ishihara, H., Kaneko, H., Hasegawa, N., Tamaura, Y., Two-step water-splitting at 1273–1623K using yttria-stabilized zirconia-iron oxide solid solution via co-precipitation and solid-state reaction. *Energy*, 33, 1788–1793, 2008.

70. Scheffe, J.R., Li, J., Weimer, A.W., A spinel ferrite/hercynite water-splitting redox cycle. *Int. J. Hydrog. Energy*, 35, 3333–3340, 2010.
71. Muhich, C.L., Evanko, B.W., Weston, K.C., Lichty, P., Liang, X., Martinek, J., Musgrave, C.B., Weimer, A.W., Efficient generation of H₂ by splitting water with an isothermal redox cycle. *Science*, 341, 540, 2013.
72. Arifin, D., Aston, V.J., Liang, X., McDaniel, A.H., Weimer, A.W., CoFe₂O₄ on a porous Al₂O₃ nanostructure for solar thermochemical CO₂ splitting. *Energy Environ. Sci.*, 5, 9438, 2012.
73. Hoskins, A.L., Millican, S.L., Czernik, C.E., Alshankiti, I., Netter, J.C., Wendelin, T.J., Musgrave, C.B., Weimer, A.W., Continuous on-sun solar thermochemical hydrogen production via an isothermal redox cycle. *Appl. Energy*, 249, 368–376, 2019.
74. Muhich, C.L., Ehrhart, B.D., Witte, V.A., Miller, S.L., Coker, E.N., Musgrave, C.B., Weimer, A.W., Predicting the solar thermochemical water splitting ability and reaction mechanism of metal oxides: A case study of the hercynite family of water splitting cycles. *Energy Environ. Sci.*, 8, 3687–3699, 2015.
75. Trottier, R.M., Bare, Z.J.L., Millican, S.L., Musgrave, C.B., Musgrave, C.B., Musgrave, C.B., Predicting spinel disorder and its effect on oxygen transport kinetics in hercynite. *ACS Appl. Mater. Interfaces*, 12, 23831–23843, 2020.
76. Al-Shankiti, I.A., Bayon, A., Weimer, A.W., Reduction kinetics of hercynite redox materials for solar thermochemical water splitting. *Chem. Eng. J. Amst. Neth.*, 389, 124429, 2020.
77. Millican, S.L., Clary, J.M., Musgrave, C.B., Lany, S., Redox defect thermochemistry of FeAl₂O₄ hercynite in water splitting from first-principles methods. *Chem. Mater.*, 34, 519, 2022.
78. Bhosale, R.R., Al Momani, F., Rashid, S., Solar thermochemical H₂ production via MnSO₄/MnO water splitting cycle: Thermodynamic equilibrium and efficiency analysis. *Int. J. Hydrog. Energy*, 45, 10324–10333, 2020.
79. Charvin, P., Abanades, S., Beche, E., Lemont, F., Flamant, G., Hydrogen production from mixed cerium oxides via three-step water-splitting cycles. *Solid State Ion.*, 180, 1003–1010, 2009.
80. Ruan, C., Tan, Y., Li, L., Wang, J., Liu, X., Wang, X., A novel CeO_{2-x}SnO₂/Ce₂Sn₂O₇ pyrochlore cycle for enhanced solar thermochemical water splitting. *AIChE J.*, 63, 3450–3462, 2017.
81. Sadeghi, S. and Ghandehariun, S., Thermodynamic analysis and optimization of an integrated solar thermochemical hydrogen production system. *Int. J. Hydrog. Energy*, 45, 28426–28436, 2020.
82. O'Brien, J.A., Hinkley, J.T., Donne, S.W., Lindquist, S.-E., The electrochemical oxidation of aqueous sulfur dioxide: A critical review of work with respect to the hybrid sulfur cycle. *Electrochim. Acta*, 55, 573–591, 2010.
83. Gorenssek, M.B., Hybrid sulfur cycle flowsheets for hydrogen production using high-temperature gas-cooled reactors. *Int. J. Hydrog. Energy*, 36, 12725–12741, 2011.

84. Allen, J.A., Rowe, G., Hinkley, J.T., Donne, S.W., Electrochemical aspects of the Hybrid Sulfur Cycle for large scale hydrogen production. *Int. J. Hydrog. Energy*, 39, 11376–11389, 2014.
85. Okeefe, D., Allen, C., Besenbruch, G., Brown, L., Norman, J., Sharp, R., Mccorkle, K., Preliminary results from bench-scale testing of a sulfur-iodine thermochemical water-splitting cycle☆. *Int. J. Hydrog. Energy*, 7, 381–392, 1982.
86. Kubo, S., Nakajima, H., Kasahara, S., Higashi, S., Masaki, T., Abe, H., Onuki, K., A demonstration study on a closed-cycle hydrogen production by the thermochemical water-splitting iodine–sulfur process. *Nucl. Eng. Des.*, 233, 347–354, 2004.
87. Goldstein, S., Borgard, J., Vitart, X., Upper bound and best estimate of the efficiency of the iodine sulphur cycle. *Int. J. Hydrog. Energy*, 30, 619–626, 2005.
88. Brown, L.C., Funk, J.F., Showalter, S.K., Initial screening of thermochemical water-splitting cycles for high efficiency generation of hydrogen fuels using nuclear power, US Department of Energy Technical Report, GA-A23373, 761610, 1999.
89. Bulfin, B., Lange, M., de Oliveira, L., Roeb, M., Sattler, C., Solar thermochemical hydrogen production using ceria zirconia solid solutions: Efficiency analysis. *Int. J. Hydrog. Energy*, 41, 19320–19328, 2016.
90. Ehrhart, B.D., Muhich, C.L., Al-Shankiti, I., Weimer, A.W., System efficiency for two-step metal oxide solar thermochemical hydrogen production-part 1: Thermodynamic model and impact of oxidation kinetics. *Int. J. Hydrog. Energy*, 41, 19881–19893, 2016.
91. Ehrhart, B.D., Muhich, C.L., Al-Shankiti, I., Weimer, A.W., System efficiency for two-step metal oxide solar thermochemical hydrogen production-part 2: Impact of gas heat recuperation and separation temperatures. *Int. J. Hydrog. Energy*, 41, 19894–19903, 2016.
92. Ehrhart, B.D., Muhich, C.L., Al-Shankiti, I., Weimer, A.W., System efficiency for two-step metal oxide solar thermochemical hydrogen production-part 3: Various methods for achieving low oxygen partial pressures in the reduction reaction. *Int. J. Hydrog. Energy*, 41, 19904–19914, 2016.
93. Brendelberger, S., Rosenstiel, A., Lopez-Roman, A., Prieto, C., Sattler, C., Performance analysis of operational strategies for monolithic receiver-reactor arrays in solar thermochemical hydrogen production plants. *Int. J. Hydrog. Energy*, 45, 26104–26116, 2020.
94. Budama, V.K., Brendelberger, S., Roeb, M., Sattler, C., Performance analysis and optimization of solar thermochemical water-splitting cycle with single and multiple receivers. *Energy Technol.*, 10, 2021.
95. Lundberg, M., Model calculations on some feasible two-step water splitting processes. *Int. J. Hydrog. Energy*, 10, 18, 369–376, 1993.

96. Siegel, N.P., Miller, J.E., Ermanoski, I., Diver, R.B., Stechel, E.B., Factors affecting the efficiency of solar driven metal oxide thermochemical cycles. *Ind. Eng. Chem. Res.*, 52, 3276–3286, 2013.
97. Meredig, B. and Wolverton, C., First-principles thermodynamic framework for the evaluation of thermochemical H₂O- or CO₂-splitting materials. *Phys. Rev. B*, 80, 245119, 2009.
98. Bayon, A., de la Calle, A., Stechel, E.B., Muhich, C., Operational limits of redox metal oxides performing thermochemical water splitting. *Energy Technol.*, 10, 2100222, 2022.
99. Li, S., Wheeler, V.M., Kreider, P.B., Lipiński, W., Thermodynamic analyses of fuel production via solar-driven non-stoichiometric metal oxide redox cycling. Part 1. Revisiting flow and equilibrium assumptions. *Energy Fuels*, 32, 10838–10847, 2018.
100. Li, S., Wheeler, V.M., Kreider, P.B., Bader, R., Lipiński, W., Thermodynamic analyses of fuel production via solar-driven non-stoichiometric metal oxide redox cycling. Part 2. Impact of solid–gas flow configurations and active material composition on system-level efficiency. *Energy Fuels*, 32, 10848–10863, 2018.
101. de la Calle, A., Ermanoski, I., Stechel, E.B., Towards chemical equilibrium in thermochemical water splitting. Part 1: Thermal reduction. *Int. J. Hydrog. Energy*, 47, 10474–10482, 2022.
102. Roeb, M., Neises, M., Monnerie, N., Call, F., Simon, H., Sattler, C., Schmücker, M., Pitz-Paal, R., Materials-related aspects of thermochemical water and carbon dioxide splitting: A review. *Materials*, 5, 2015–2054, 2012.
103. D'Souza, L., Thermochemical hydrogen production from water using reducible oxide materials: A critical review. *Mater. Renew. Sustain. Energy*, 2, 7, 2013.
104. Carrillo, R.J. and Scheffe, J.R., Advances and trends in redox materials for solar thermochemical fuel production. *Sol. Energy*, 156, 3–20, 2017.
105. Scheffe, J.R., Weibel, D., Steinfeld, A., Lanthanum–strontium–manganese perovskites as redox materials for solar thermochemical splitting of H₂O and CO₂. *Energy Fuels*, 27, 4250–4257, 2013.
106. Merkulov, O.V., Markov, A.A., Leonidov, I.A., Patrakeev, M.V., Kozhevnikov, V.L., Oxygen nonstoichiometry and thermodynamic quantities in solid solution SrFe_{1-x}Sn_xO_{3-δ}. *J. Solid State Chem.*, 262, 121–126, 2018.
107. Bulfin, B., Call, F., Lange, M., Lübber, O., Sattler, C., Pitz-Paal, R., Shvets, I.V., Thermodynamics of CeO₂ thermochemical fuel production. *Energy Fuels*, 29, 1001–1009, 2015.
108. Vieten, J., Bulfin, B., Huck, P., Horton, M., Guban, D., Zhu, L., Lu, Y., Persson, K.A., Roeb, M., Sattler, C., Materials design of perovskite solid solutions for thermochemical applications. *Energy Environ. Sci.*, 12, 1369–1384, 2019.
109. Tagawa, H., Oxygen nonstoichiometry in perovskite-type oxide, undoped and Sr-doped LaMnO₃. *ECS Proc.*, Vol., 1997–40, 785–794, 1997.

110. Miller, J.E., Allendorf, M.D., Diver, R.B., Evans, L.R., Siegel, N.P., Stuecker, J.N., Metal oxide composites and structures for ultra-high temperature solar thermochemical cycles. *J. Mater. Sci.*, 43, 4714–4728, 2008.
111. Abanades, S., Legal, A., Cordier, A., Peraudeau, G., Flamant, G., & Julbe, A., Investigation of reactive cerium-based oxides for H₂ production by thermochemical two-step water-splitting. *J. Mater. Sci.*, 45, 4163–4173, 2010.
112. Bulfin, B., Call, F., Vieten, J., Roeb, M., Sattler, C., Shvets, I.V., Oxidation and reduction reaction kinetics of mixed cerium zirconium oxides. *J. Phys. Chem. C*, 120, 2027–2035, 2016.
113. Fedunik-Hofman, L., Bayon, A., Donne, S.W., Kinetics of solid-gas reactions and their application to carbonate looping systems. *Energies*, 12, 2981, 2019.
114. Irvine, J., Rupp, J.L.M., Liu, G., Xu, X., Haile, S., Qian, X., Snyder, A., Freer, R., Ekren, D., Skinner, S., Celikbilek, O., Chen, S., Tao, S., Shin, T.H., O’Hayre, R., Huang, J., Duan, C., Papac, M., Li, S., Celorrio, V., Russell, A., Hayden, B., Nolan, H., Huang, X., Wang, G., Metcalfe, I., Neagu, D., Martín, S.G., Roadmap on inorganic perovskites for energy applications. *J. Phys. Energy*, 3, 031502, 2021.
115. Davenport, T.C., Yang, C.-K., Kucharczyk, C.J., Ignatowich, M.J., Haile, S.M., Maximizing fuel production rates in isothermal solar thermochemical fuel production. *Appl. Energy*, 183, 1098–1111, 2016.
116. Ignatowich, M.J., Bork, A.H., Davenport, T.C., Rupp, J.L.M., Yang, C., Yamazaki, Y., Haile, S.M., Impact of enhanced oxide reducibility on rates of solar-driven thermochemical fuel production. *MRS Commun.*, 7, 873–878, 2017.
117. Ermanoski, I., Siegel, N.P., Stechel, E.B., A new reactor concept for efficient solar-thermochemical fuel production. *J. Sol. Energy Eng.*, 135, 031002, 2013.
118. Falter, C. and Sizmann, A., Solar thermochemical hydrogen production in the USA. *Sustainability*, 13, 7804, 2021.
119. Budama, V.K., Johnson, N.G., Ermanoski, I., Stechel, E.B., Techno-economic analysis of thermochemical water-splitting system for co-production of hydrogen and electricity. *Int. J. Hydrog. Energy*, 46, 1656–1670, 2021.
120. Michalsky, R., Botu, V., Hargus, C.M., Peterson, A.A., Steinfeld, A., Design principles for metal oxide redox materials for solar-driven isothermal fuel production. *Adv. Energy Mater.*, 5, 1401082, 2014.
121. Warren, K.J., Tran, J.T., Weimer, A.W., A thermochemical study of iron aluminate-based materials: A preferred class for isothermal water splitting. *Energy Environ. Sci.*, 15, 2022.
122. Roeb, M. and Sattler, C., Isothermal water splitting. *Science*, 341, 470–471, 2013.
123. Ceperley, D.M. and Alder, B.J., Ground state of the electron gas by a stochastic method. *Phys. Rev. Lett.*, 45, 566–569, 1980.
124. Perdew, J.P. and Zunger, A., Self-interaction correction to density-functional approximations for many-electron systems. *Phys. Rev. B*, 23, 5048–5079, 1981.

125. Perdew, J.P. and Wang, Y., Accurate and simple analytic representation of the electron-gas correlation energy. *Phys. Rev. B*, 45, 13244–13249, 1992.
126. Perdew, J.P., Burke, K., Ernzerhof, M., Generalized gradient approximation made simple. *Phys. Rev. Lett.*, 77, 3865–3868, 1996.
127. Sun, J., Ruzsinszky, A., Perdew, J.P., Strongly constrained and appropriately normed semilocal density functional. *Phys. Rev. Lett.*, 115, 036402, 2015.
128. Dudarev, S.L., Botton, G.A., Savrasov, S.Y., Humphreys, C.J., Sutton, A.P., Electron-energy-loss spectra and the structural stability of nickel oxide: An LSDA+U study. *Phys. Rev. B*, 57, 1505–1509, 1998.
129. Wang, L., Maxisch, T., Ceder, G., Oxidation energies of transition metal oxides within the GGA+U framework. *Phys. Rev. B*, 73, 195107, 2006.
130. Sai Gautam, G. and Carter, E.A., Evaluating transition metal oxides within DFT-SCAN and SCAN+U frameworks for solar thermochemical applications. *Phys. Rev. Mater.*, 2, 095401, 2018.
131. Long, O.Y., Sai Gautam, G., Carter, E.A., Evaluating optimal U for 3d transition-metal oxides within the SCAN+U framework. *Phys. Rev. Mater.*, 4, 045401, 2020.
132. Wexler, R.B., Gautam, G.S., Carter, E.A., Exchange-correlation functional challenges in modeling quaternary chalcogenides. *Phys. Rev. B*, 102, 054101, 2020.
133. Lany, S., Communication: The electronic entropy of charged defect formation and its impact on thermochemical redox cycles. *J. Chem. Phys.*, 148, 071101, 2018.
134. Pastor, E., Sachs, M., Selim, S., Durrant, J.R., Bakulin, A.A., Walsh, A., Electronic defects in metal oxide photocatalysts. *Nat. Rev. Mater.*, 7, 503, 2022.
135. Freysoldt, C., Neugebauer, J., Van de Walle, C.G., Fully Ab initio finite-size corrections for charged-defect supercell calculations. *Phys. Rev. Lett.*, 102, 016402, 2009.
136. Kumagai, Y. and Oba, F., Electrostatics-based finite-size corrections for first-principles point defect calculations. *Phys. Rev. B*, 89, 195205, 2014.
137. Walsh, A., Correcting the corrections for charged defects in crystals. *NPJ Comput. Mater.*, 7, 72, 2021.
138. Stevanović, V., Lany, S., Zhang, X., Zunger, A., Correcting density functional theory for accurate predictions of compound enthalpies of formation: Fitted elemental-phase reference energies. *Phys. Rev. B*, 85, 115104, 2012.
139. Yu, K. and Carter, E.A., Communication: Comparing ab initio methods of obtaining effective U parameters for closed-shell materials. *J. Chem. Phys.*, 140, 121105, 2014.
140. Loschen, C., Carrasco, J., Neyman, K.M., Illas, F., First-principles LDA + U and GGA + U study of cerium oxides: Dependence on the effective U parameter. *Phys. Rev. B*, 75, 035115, 2007.

141. Da Silva, J.L.F., Ganduglia-Pirovano, M.V., Sauer, J., Bayer, V., Kresse, G., Hybrid functionals applied to rare-earth oxides: The example of ceria. *Phys. Rev. B*, 75, 045121, 2007.
142. Chase Jr., M.W., NIST-JANAF thermochemical tables. *J. Phys. Chem. Ref. Data Monogr.*, 9, 1998.
143. Wu, X., Vanderbilt, D., Hamann, D.R., Systematic treatment of displacements, strains, and electric fields in density-functional perturbation theory. *Phys. Rev. B*, 72, 035105, 2005.
144. Grieshammer, S., Zacherle, T., Martin, M., Entropies of defect formation in ceria from first principles. *Phys. Chem. Chem. Phys.*, 15, 15935–15942, 2013.
145. Campañá, C. and Müser, M.H., Practical Green's function approach to the simulation of elastic semi-infinite solids. *Phys. Rev. B*, 74, 075420, 2006.
146. Kong, L.T., Bartels, G., Campañá, C., Denniston, C., Müser, M.H., Implementation of Green's function molecular dynamics: An extension to LAMMPS. *Comput. Phys. Commun.*, 180, 1004–1010, 2009.
147. Kong, L.T., Denniston, C., Müser, M.H., An improved version of the Green's function molecular dynamics method. *Comput. Phys. Commun.*, 182, 540–541, 2011.
148. Kong, L.T., Phonon dispersion measured directly from molecular dynamics simulations. *Comput. Phys. Commun.*, 182, 2201–2207, 2011.
149. Sai Gautam, G., Stechel, E.B., Carter, E.A., A first-principles-based sub-lattice formalism for predicting off-stoichiometry in materials for solar thermochemical applications: The example of ceria. *Adv. Theory Simul.*, 3, 2000112, 2020.
150. Zinkevich, M., Djurovic, D., Aldinger, F., Thermodynamic modelling of the cerium–oxygen system. *Solid State Ion.*, 177, 989–1001, 2006.
151. Hillert, M., The compound energy formalism. *J. Alloys Compd.*, 320, 161–176, 2001.
152. Gopal, C.B. and van de Walle, A., Ab initio thermodynamics of intrinsic oxygen vacancies in ceria. *Phys. Rev. B*, 86, 134117, 2012.
153. van de Walle, A. and Asta, M., Self-driven lattice-model Monte Carlo simulations of alloy thermodynamic properties and phase diagrams. *Modelling Simul. Mater. Sci. Eng.*, 10, 521, 2002.
154. Ling, S., High-concentration point-defect chemistry: Statistical-thermodynamic approach applied to nonstoichiometric cerium dioxides. *Phys. Rev. B*, 49, 864–880, 1994.
155. Zhou, F. and Åberg, D., Crystal-field calculations for transition-metal ions by application of an opposing potential. *Phys. Rev. B*, 93, 085123, 2016.
156. Naghavi, S.S., Emery, A.A., Hansen, H.A., Zhou, F., Ozolins, V., Wolverton, C., Giant onsite electronic entropy enhances the performance of ceria for water splitting. *Nat. Commun.*, 8, 285, 2017.
157. Panlener, R.J., Blumenthal, R.N., Garnier, J.E., A thermodynamic study of nonstoichiometric cerium dioxide. *J. Phys. Chem. Solids*, 36, 1213–1222, 1975.

158. Ong, S.P., Wang, L., Kang, B., Ceder, G., Li-Fe-P-O₂ phase diagram from first principles calculations. *Chem. Mater.*, 20, 1798–1807, 2008.
159. Ong, S.P., Jain, A., Hautier, G., Kang, B., Ceder, G., Thermal stabilities of delithiated olivine MPO₄ (M=Fe, Mn) cathodes investigated using first principles calculations. *Electrochem. Commun.*, 12, 427–430, 2010.
160. Zunger, A., Wei, S.-H., Ferreira, L.G., Bernard, J.E., Special quasirandom structures. *Phys. Rev. Lett.*, 65, 353–356, 1990.
161. van de Walle, A., Tiwary, P., de Jong, M., Olmsted, D.L., Asta, M., Dick, A., Shin, D., Wang, Y., Chen, L.-Q., Liu, Z.-K., Efficient stochastic generation of special quasirandom structures. *Calphad*, 42, 13–18, 2013.
162. van de Walle, A., Multicomponent multisublattice alloys, nonconfigurational entropy and other additions to the alloy theoretic automated toolkit. *Calphad*, 33, 266–278, 2009.
163. Raybaud, P., Digne, M., Iftimie, R., Wellens, W., Euzen, P., Toulhoat, H., Morphology and surface properties of boehmite (γ -AlOOH): A density functional theory study. *J. Catal.*, 201, 236–246, 2001.
164. Gong, X.-Q. and Selloni, A., Reactivity of anatase TiO₂ nanoparticles: The role of the minority (001) surface. *J. Phys. Chem. B*, 109, 19560–19562, 2005.
165. Wexler, R.B. and Sohlberg, K., Role of proton hopping in surface charge transport on tin dioxide as revealed by the thermal dependence of conductance. *J. Phys. Chem. A*, 118, 12031–12040, 2014.
166. Mills, G., Jónsson, H., Schenter, G.K., Reversible work transition state theory: application to dissociative adsorption of hydrogen. *Surf. Sci.*, 324, 305–337, 1995.
167. Henkelman, G. and Jónsson, H., Improved tangent estimate in the nudged elastic band method for finding minimum energy paths and saddle points. *J. Chem. Phys.*, 113, 9978–9985, 2000.
168. Henkelman, G., Uberuaga, B.P., Jónsson, H., A climbing image nudged elastic band method for finding saddle points and minimum energy paths. *J. Chem. Phys.*, 113, 9901–9904, 2000.
169. Trottier, R.M., Millican, S.L., Musgrave, C.B., Musgrave, C.B., Musgrave, C.B., Modified single iteration synchronous-transit approach to bound diffusion barriers for solid-state reactions. *J. Chem. Theory Comput.*, 16, 5912–5922, 2020.
170. Caspersen, K.J. and Carter, E.A., Finding transition states for crystalline solid-solid phase transformations. *Proc. Natl. Acad. Sci.*, 102, 6738–6743, 2005.
171. Xu, R. and Wiesner, T.F., Dynamic model of a solar thermochemical water-splitting reactor with integrated energy collection and storage. *Int. J. Hydrog. Energy*, 37, 2210–2223, 2012.
172. Chueh, W.C., Falter, C., Abbott, M., Scipio, D., Furler, P., Haile, S.M., Steinfeld, A., High-flux solar-driven thermochemical dissociation of CO₂ and H₂O using nonstoichiometric ceria. *Science*, 330, 1797, 2010.

173. Arifin, D. and Weimer, A.W., Kinetics and mechanism of solar-thermochemical H₂ and CO production by oxidation of reduced CeO₂. *Sol. Energy*, 160, 178–185, 2017.
174. Bhosale, R.R., Takalkar, G., Sutar, P., Kumar, A., AlMomani, F., Khraisheh, M., A decade of ceria based solar thermochemical H₂O/CO₂ splitting cycle. *Int. J. Hydrog. Energy*, 44, 34–60, 2019.
175. Le Gal, A. and Abanades, S., Dopant incorporation in ceria for enhanced water-splitting activity during solar thermochemical hydrogen generation. *J. Phys. Chem. C*, 116, 13516–13523, 2012.
176. Costa Oliveira, F.A., Barreiros, M.A., Haeussler, A., Caetano, A.P.F., Mouquinho, A., II, Oliveira e. Silva, P.M., Novais, R.M., Pullar, R.C., Abanades, S., High performance cork-templated ceria for solar thermochemical hydrogen production via two-step water-splitting cycles. *Sustain. Energy Fuels*, 4, 3077–3089, 2020.
177. Ganzoury, M.A., Fateen, S.-E.K., El Sheltawy, S.T., Radwan, A.M., Allam, N.K., Thermodynamic and efficiency analysis of solar thermochemical water splitting using Ce-Zr mixtures. *Sol. Energy*, 135, 154–162, 2016.
178. Kaneko, H., Miura, T., Ishihara, H., Taku, S., Yokoyama, T., Nakajima, H., Tamaura, Y., Reactive ceramics of CeO₂-MO_x (M=Mn, Fe, Ni, Cu) for H₂ generation by two-step water splitting using concentrated solar thermal energy. *Energy*, 32, 656–663, 2007.
179. Ackermann, S., Scheffe, J.R., Steinfeld, A., Diffusion of oxygen in ceria at elevated temperatures and its application to H₂O/CO₂ splitting thermochemical redox cycles. *J. Phys. Chem. C*, 118, 5216–5225, 2014.
180. Muhich, C., Hoes, M., Steinfeld, A., Mimicking tetravalent dopant behavior using paired charge compensating dopants to improve the redox performance of ceria for thermochemically splitting H₂O and CO₂. *Acta Mater.*, 144, 728–737, 2018.
181. Furler, P., Scheffe, J.R., Steinfeld, A., Syngas production by simultaneous splitting of H₂O and CO₂ via ceria redox reactions in a high-temperature solar reactor. *Energy Env. Sci.*, 5, 6098–6103, 2011.
182. Hao, Y., Yang, C.-K., Haile, S.M., High-temperature isothermal chemical cycling for solar-driven fuel production. *Phys. Chem. Chem. Phys.*, 15, 17084–17092, 2013.
183. Chueh, W.C. and Haile, S.M., Ceria as a thermochemical reaction medium for selectively generating syngas or methane from H₂O and CO₂. *ChemSusChem*, 2, 735–739, 2009.
184. Chueh, W.C. and Haile, S.M., A thermochemical study of ceria: Exploiting an old material for new modes of energy conversion and CO₂ mitigation. *Philos. Trans. R. Soc. Math. Phys. Eng. Sci.*, 368, 3269–3294, 2010.
185. Marxer, D., Furler, P., Scheffe, J., Geerlings, H., Falter, C., Batteiger, V., Sizmann, A., Steinfeld, A., Demonstration of the entire production chain to renewable kerosene via solar thermochemical splitting of H₂O and CO₂. *Energy Fuels*, 29, 3241–3250, 2015.

186. Reinhardt, K. and Winkler, H., *Ullmann's Encyclopedia of Industrial Chemistry*, Wiley-VCH Verlag GmbH & Co. KGaA (Ed.), Wiley-VCH Verlag GmbH & Co. KGaA, Hoboken, New Jersey, 2000.
187. Bulfin, B., Hoffmann, L., Oliveira, L., Knoblauch, N., Call, F., Roeb, M., Sattler, C., Schmücker, M., Statistical thermodynamics of non-stoichiometric ceria and ceria zirconia solid solutions. *Phys. Chem. Chem. Phys.*, 18, 23147–23154, 2016.
188. Takalkar, G., Bhosale, R.R., Rashid, S., AlMomani, F., Shakoor, R.A., Al Ashraf, A., Application of Li-, Mg-, Ba-, Sr-, Ca-, and Sn-doped ceria for solar-driven thermochemical conversion of carbon dioxide. *J. Mater. Sci.*, 55, 11797–11807, 2020.
189. Meng, Q.-L., Lee, C., Shigeta, S., Kaneko, H., Tamaura, Y., Solar hydrogen production using $\text{Ce}_{1-x}\text{Li}_x\text{O}_{2-\delta}$ solid solutions via a thermochemical, two-step water-splitting cycle. *J. Solid State Chem.*, 194, 343–351, 2012.
190. Portarapillo, M., Russo, D., Landi, G., Luciani, G., Di Benedetto, A., K-doped $\text{CeO}_2\text{-ZrO}_2$ for CO_2 thermochemical catalytic splitting. *RSC Adv.*, 11, 39420–39427, 2022.
191. Bonk, A., Maier, A.C., Schlupp, M.V.F., Burnat, D., Remhof, A., Delmelle, R., Steinfeld, A., Vogt, U.F., The effect of dopants on the redox performance, microstructure and phase formation of ceria. *J. Power Sources*, 300, 261–271, 2015.
192. Meng, Q.-L., Lee, C., Ishihara, T., Kaneko, H., Tamaura, Y., Reactivity of CeO_2 -based ceramics for solar hydrogen production via a two-step water-splitting cycle with concentrated solar energy. *Int. J. Hydrog. Energy*, 36, 13435–13441, 2011.
193. Scheffe, J.R. and Steinfeld, A., Thermodynamic analysis of cerium-based oxides for solar thermochemical fuel production. *Energy Fuels*, 26, 1928–1936, 2012.
194. Liu, Z., Ma, H., Sorrell, C.C., Koshy, P., Hart, J.N., *Enhancement of Light Absorption and Oxygen Vacancy Formation in CeO_2 by Transition Metal Doping: A DFT Study*, 2022, arXiv:2012.06195.
195. Nair, M.M. and Abanades, S., Tailoring hybrid nonstoichiometric ceria redox cycle for combined solar methane reforming and thermochemical conversion of $\text{H}_2\text{O}/\text{CO}_2$. *Energy Fuels*, 30, 6050–6058, 2016.
196. Le Gal, A., Abanades, S., Bion, N., Le Mercier, T., Harle, V., Reactivity of doped ceria-based mixed oxides for solar thermochemical hydrogen generation via two-step water-splitting cycles. *Energy Fuels*, 27, 6068–6078, 2013.
197. Call, F., Roeb, M., Schmücker, M., Sattler, C., Pitz-Paal, R., Ceria doped with zirconium and lanthanide oxides to enhance solar thermochemical production of fuels. *J. Phys. Chem. C*, 119, 6929–6938, 2015.
198. Scheffe, J.R., Jacot, R., Patzke, G.R., Steinfeld, A., Synthesis, characterization, and thermochemical redox performance of Hf^{4+} , Zr^{4+} , and Sc^{3+} doped ceria for splitting CO_2 . *J. Phys. Chem. C*, 117, 24104–24114, 2013.

199. Hao, Y., Yang, C.-K., Haile, S.M., Ceria-zirconia solid solutions ($\text{Ce}_{1-x}\text{Zr}_x\text{O}_{2-\delta}$, $x \leq 0.2$) for solar thermochemical water splitting: A thermodynamic study. *Chem. Mater.*, 26, 6073–6082, 2014.
200. Rothensteiner, M., Bonk, A., Vogt, U.F., Emerich, H., van Bokhoven, J.A., Structural changes in $\text{Ce}_{0.5}\text{Zr}_{0.5}\text{O}_{2-\delta}$ under temperature-swing and isothermal solar thermochemical looping conditions determined by *in situ* Ce K and Zr K edge x-ray absorption spectroscopy. *J. Phys. Chem. C*, 120, 13931–13941, 2016.
201. Petkovich, N.D., Rudisill, S.G., Venstrom, L.J., Boman, D.B., Davidson, J.H., Stein, A., Control of heterogeneity in nanostructured $\text{Ce}_{1-x}\text{Zr}_x\text{O}_2$ binary oxides for enhanced thermal stability and water splitting activity. *J. Phys. Chem. C*, 115, 21022–21033, 2011.
202. Riaz, A., Kremer, F., Kim, T., Sattayaporn, S., Tsuzuki, T., Lipiński, W., Lowe, A., Experimental demonstration of vanadium-doped nanostructured ceria for enhanced solar thermochemical syngas production. *Nano Energy*, 81, 105639, 2021.
203. Singh, P. and Hegde, M.S., $\text{Ce}_{0.67}\text{Cr}_{0.33}\text{O}_{2.11}$: A new low-temperature O_2 evolution material and H_2 generation catalyst by thermochemical splitting of water. *Chem. Mater.*, 22, 762–768, 2010.
204. Kaneko, H., Ishihara, H., Taku, S., Naganuma, Y., Hasegawa, N., Tamaura, Y., Cerium ion redox system in $\text{CeO}_{2-x}\text{Fe}_2\text{O}_3$ solid solution at high temperatures (1,273–1,673 K) in the two-step water-splitting reaction for solar H_2 generation. *J. Mater. Sci.*, 43, 3153–3161, 2008.
205. Kaneko, H. and Tamaura, Y., Reactivity and XAFS study on $(1-x)\text{CeO}_2-x\text{NiO}$ ($x=0.025-0.3$) system in the two-step water-splitting reaction for solar H_2 production. *J. Phys. Chem. Solids*, 70, 1008–1014, 2009.
206. Lin, F., Rothensteiner, M., Alxneit, I., van Bokhoven, J.A., Wokaun, A., First demonstration of direct hydrocarbon fuel production from water and carbon dioxide by solar-driven thermochemical cycles using rhodium-ceria. *Energy Environ. Sci.*, 9, 2400–2409, 2016.
207. Muhich, C. and Steinfeld, A., Principles of doping ceria for the solar thermochemical redox splitting of H_2O and CO_2 . *J. Mater. Chem. Mater. Energy Sustain.*, 5, 15578–15590, 2017.
208. Nolan, M., Enhanced oxygen vacancy formation in ceria (111) and (110) surfaces doped with divalent cations. *J. Mater. Chem.*, 21, 9160, 2011.
209. Nakayama, M. and Martin, M., First-principles study on defect chemistry and migration of oxide ions in ceria doped with rare-earth cations. *Phys. Chem. Chem. Phys.*, 11, 3241, 2009.
210. Scanlon, D.O., Morgan, B.J., Watson, G.W., The origin of the enhanced oxygen storage capacity of $\text{Ce}_{1-x}(\text{Pd/Pt})_x\text{O}_2$. *Phys. Chem. Chem. Phys.*, 13, 4279, 2011.
211. Wexler, R.B., Gautam, G.S., Carter, E.A., Optimizing kesterite solar cells from $\text{Cu}_2\text{ZnSnS}_4$ to $\text{Cu}_2\text{CdGe}(\text{S}, \text{Se})_4$. *J. Mater. Chem. A*, 9, 9882–9897, 2021.

212. Wexler, R.B., Gautam, G.S., Stechel, E.B., Carter, E.A., Factors governing oxygen vacancy formation in oxide perovskites. *J. Am. Chem. Soc.*, 143, 13212–13227, 2021.
213. Dawicke, J.W. and Blumenthal, R.N., Oxygen association pressure measurements on nonstoichiometric cerium dioxide. *J. Electrochem. Soc.*, 133, 904–909, 1986.
214. Bulfin, B., Lowe, A.J., Keogh, K.A., Murphy, B.E., Lübben, O., Krasnikov, S.A., Shvets, I.V., Analytical model of CeO_2 oxidation and reduction. *J. Phys. Chem. C*, 117, 24129–24137, 2013.
215. Fu, M., Xu, H., Li, X., Mechanism of oxygen vacancy assisted water-splitting of LaMnO_3 : Inorganic perovskite prediction for fast solar thermochemical H_2 production. *Inorg. Chem. Front.*, 7, 2381–2387, 2020.
216. Demont, A., Abanades, S., Beche, E., Investigation of perovskite structures as oxygen-exchange redox materials for hydrogen production from thermochemical two-step water-splitting cycles. *J. Phys. Chem. C*, 118, 12682–12692, 2014.
217. Bakken, E., Norby, T., Stølen, S., Redox energetics of perovskite-related oxides. *J. Mater. Chem.*, 12, 317–323, 2002.
218. McDaniel, A.H., Miller, E.C., Arifin, D., Ambrosini, A., Coker, E.N., O'Hayre, R., Chueh, W.C., Tong, J., Sr- and Mn-doped $\text{LaAlO}_{3-\delta}$ for solar thermochemical H_2 and CO production. *Energy Environ. Sci.*, 6, 2424–2428, 2013.
219. McDaniel, A.H., Ambrosini, A., Coker, E.N., Miller, J.E., Chueh, W.C., O'Hayre, R., Tong, J., Nonstoichiometric perovskite oxides for solar thermochemical H_2 and CO production. *Energy Procedia*, 49, 2009–2018, 2014.
220. Deml, A.M., Stevanović, V., Holder, A.M., Sanders, M., O'Hayre, R., Musgrave, C.B., Tunable oxygen vacancy formation energetics in the complex perovskite oxide $\text{Sr}_x\text{La}_{1-x}\text{Mn}_y\text{Al}_{1-y}\text{O}_3$. *Chem. Mater.*, 26, 6595–6602, 2014.
221. Takacs, M., Hoes, M., Caduff, M., Cooper, T., Scheffe, J.R., Steinfeld, A., Oxygen nonstoichiometry, defect equilibria, and thermodynamic characterization of LaMnO_3 perovskites with Ca/Sr A-site and Al B-site doping. *Acta Mater.*, 103, 700–710, 2016.
222. Cooper, T., Scheffe, J.R., Galvez, M.E., Jacot, R., Patzke, G., Steinfeld, A., Lanthanum manganite perovskites with Ca/Sr A-site and Al B-site doping as effective oxygen exchange materials for solar thermochemical fuel production. *Energy Technol.*, 3, 1130–1142, 2015.
223. Wang, L., Al-Mamun, M., Liu, P., Wang, Y., Gui Yang, H., Zhao, H., $\text{La}_{1-x}\text{Ca}_x\text{Mn}_{1-y}\text{Al}_y\text{O}_3$ perovskites as efficient catalysts for two-step thermochemical water splitting in conjunction with exceptional hydrogen yields. *Chin. J. Catal.*, 38, 1079–1086, 2017.
224. Luciani, G., Landi, G., Aronne, A., Di Benedetto, A., Partial substitution of B cation in $\text{La}_{0.6}\text{Sr}_{0.4}\text{MnO}_3$ perovskites: A promising strategy to improve the redox properties useful for solar thermochemical water and carbon dioxide splitting. *Sol. Energy*, 171, 1–7, 2018.

225. Chen, Z., Jiang, Q., Cheng, F., Tong, J., Yang, M., Jiang, Z., Li, C., Sr- and Co-doped $\text{LaGaO}_{3-\delta}$ with high O_2 and H_2 yields in solar thermochemical water splitting. *J. Mater. Chem. Mater. Energy Sustain.*, 7, 6099–6112, 2019.
226. Barcellos, D.R., Sanders, M.D., Tong, J., McDaniel, A.H., O'Hayre, R.P., $\text{BaCe}_{0.25}\text{Mn}_{0.75}\text{O}_{3-\delta}$, a promising perovskite-type oxide for solar thermochemical hydrogen production. *Energy Environ. Sci.*, 11, 3256–3265, 2018.
227. Qian, X., He, J., Mastronardo, E., Baldassarri, B., Wolverson, C., Haile, S.M., Favorable redox thermodynamics of $\text{SrTi}_{0.5}\text{Mn}_{0.5}\text{O}_{3-\delta}$ in solar thermochemical water splitting. *Chem. Mater.*, 32, 9335–9346, 2020.
228. Sai Gautam, G., Stechel, E.B., Carter, E.A., Exploring Ca-Ce-M-O (M = 3d transition metal) oxide perovskites for solar thermochemical applications. *Chem. Mater.*, 32, 9964–9982, 2020.
229. Wexler, R. B., Gautam, G. S., Bell, R., Shulda, S., Strange, N. A., Trindell, J. A., Sugar, J. D., Nygren, E., Sainio, S., McDaniel, A. H., Ginley, D., Carter, E. A., Stechel, E. B., Multiple and nonlocal cation redox in Ca-Ce-Ti-Mn oxide perovskites for solar thermochemical applications, *Energy Environ. Sci.*, 2023.
230. Heo, S.J., Sanders, M., O'Hayre, R., Zakutayev, A., Double-site substitution of Ce into (Ba, Sr) MnO_3 perovskites for solar thermochemical hydrogen production. *ACS Energy Lett.*, 6, 3037–3043, 2021.
231. Dey, S., Naidu, B.S., Rao, C.N.R., $\text{Ln}_{0.5}\text{A}_{0.5}\text{MnO}_3$ (Ln = Lanthanide, A = Ca, Sr) perovskites exhibiting remarkable performance in the thermochemical generation of CO and H_2 from CO_2 and H_2O . *Chem.-Eur. J.*, 21, 7077–7081, 2015.
232. Barcellos, D.R., Coury, F.G., Emery, A., Sanders, M., Tong, J., McDaniel, A., Wolverson, C., Kaufman, M., O'Hayre, R., Phase identification of the layered perovskite $\text{Ce}_x\text{Sr}_{2-x}\text{MnO}_4$ and application for solar thermochemical water splitting. *Inorg. Chem.*, 58, 12, 7705, 2019.
233. Bergeson-Keller, A.M., Sanders, M.D., O'Hayre, R.P., Reduction thermodynamics of $\text{Sr}_{1-x}\text{Ce}_x\text{MnO}_3$ and $\text{Ce}_x\text{Sr}_{2-x}\text{MnO}_4$ perovskites for solar thermochemical hydrogen production. *Energy Technol.*, 10, 2100515, 2021.
234. Kubicek, M., Bork, A.H., Rupp, J.L.M., Perovskite oxides—A review on a versatile material class for solar-to-fuel conversion processes. *J. Mater. Chem. A*, 5, 11983–12000, 2017.
235. Haeussler, A., Abanades, S., Jouannaux, J., Julbe, A., Non-stoichiometric redox active perovskite materials for solar thermochemical fuel production: A review. *Catalysts*, 8, 611, 2018.
236. Emery, A.A., Saal, J.E., Kirklin, S., Hegde, V., II, Wolverson, C., High-throughput computational screening of perovskites for thermochemical water splitting applications. *Chem. Mater.*, 28, 5621–5634, 2016.
237. Ezbiri, M., Allen, K.M., Galvez, M.E., Michalsky, R., Steinfeld, A., Design principles of perovskites for thermochemical oxygen separation. *ChemSusChem*, 8, 1966–1971, 2015.

238. Deml, A.M., Holder, A.M., O'Hayre, R.P., Musgrave, C.B., Stevanović, V., Intrinsic material properties dictating oxygen vacancy formation energetics in metal oxides. *J. Phys. Chem. Lett.*, 6, 1948–1953, 2015.
239. Muñoz-García, A.B., Ritzmann, A.M., Pavone, M., Keith, J.A., Carter, E.A., Oxygen transport in perovskite-type solid oxide fuel cell materials: Insights from quantum mechanics. *Acc. Chem. Res.*, 47, 3340–3348, 2014.
240. Pavone, M., Ritzmann, A.M., Carter, E.A., Quantum-mechanics-based design principles for solid oxide fuel cell cathode materials. *Energy Environ. Sci.*, 4, 4933, 2011.
241. Zeng, Z., Calle-Vallejo, F., Mogensen, M.B., Rossmeisl, J., Generalized trends in the formation energies of perovskite oxides. *Phys. Chem. Chem. Phys.*, 15, 7526–7533, 2013.
242. Jain, A., Ong, S.P., Hautier, G., Chen, W., Richards, W.D., Dacek, S., Cholia, S., Gunter, D., Skinner, D., Ceder, G., Persson, K.A., Commentary: The materials project: A materials genome approach to accelerating materials innovation. *APL Mater.*, 1, 011002, 2013.
243. Jain, A., Hautier, G., Ong, S.P., Moore, C.J., Fischer, C.C., Persson, K.A., Ceder, G., Formation enthalpies by mixing GGA and GGA + U calculations. *Phys. Rev. B*, 84, 045115, 2011.
244. Naghavi, S.S., He, J., Wolverton, C., CeTi₂O₆-a promising oxide for solar thermochemical hydrogen production. *ACS Appl. Mater. Interfaces*, 12, 21521–21527, 2020.
245. Kramida, A., Ralchenko, Y., Reader, J., NIST ASD Team, *NIST Atomic Spectra Database (Version 5.9)*, National Institute of Standards and Technology, Gaithersburg, MD, 2021, <https://physics.nist.gov/asd>.
246. Yen, W.M., General Factors Governing the efficiency of luminescent devices. *Phys. Solid State*, 47, 1393, 2005.
247. Murgida, G.E., Ferrari, V., Ganduglia-Pirovano, M.V., Llois, A.M., Ordering of oxygen vacancies and excess charge localization in bulk ceria: A DFT + U study. *Phys. Rev. B*, 90, 115120, 2014.
248. Pártay, L.B., Csányi, G., Bernstein, N., Nested sampling for materials. *Eur. Phys. J. B*, 94, 159, 2021.
249. Deringer, V.L., Caro, M.A., Csányi, G., Machine learning interatomic potentials as emerging tools for materials science. *Adv. Mater.*, 31, 1902765, 2019.
250. Virtanen, P., Gommers, R., Oliphant, T.E., Haberland, M., Reddy, T., Cournapeau, D., Burovski, E., Peterson, P., Weckesser, W., Bright, J., van der Walt, S.J., Brett, M., Wilson, J., Millman, K.J., Mayorov, N., Nelson, A.R.J., Jones, E., Kern, R., Larson, E., Carey, C.J., Polat, Í., Feng, Y., Moore, E.W., VanderPlas, J., Laxalde, D., Perktold, J., Cimrman, R., Henriksen, I., Quintero, E.A., Harris, C.R., Archibald, A.M., Ribeiro, A.H., Pedregosa, F., van Mulbregt, P., SciPy 1.0 Contributors, SciPy 1.0: Fundamental algorithms for scientific computing in python. *Nat. Methods*, 17, 261–272, 2020.